Unified treatment of microscopic boundary conditions and efficient algorithms for estimating tangent operators of the homogenized behavior in the computational homogenization method

Van-Dung Nguyen · Ling Wu · Ludovic Noels

Abstract This work provides a unified treatment of arbitrary kinds of microscopic boundary conditions usually considered in the multi-scale computational homogenization method for nonlinear multi-physics problems. An efficient procedure is developed to enforce the multi-point linear constraints arising from the microscopic boundary condition either by the direct constraint elimination or by the Lagrange multiplier elimination methods. The macroscopic tangent operators are computed in an efficient way from a multiple right hand sides linear system whose left hand side matrix is the stiffness matrix of the microscopic linearized system at the converged solution. The number of vectors at the right hand side is equal to the number of the macroscopic kinematic variables used to formulate the microscopic boundary condition. As the resolution of the microscopic linearized system often follows a direct factorization procedure, the computation of the macroscopic tangent operators is then performed using this factorized matrix at a reduced computational time.

1 Introduction

The complex microstructure of heterogeneous materials and the complex physical behaviors of their constituents lead to a complex physical response at the structural scale. The accurate evaluation of the microstructure evolution is mandatory to predict the structural response and to allow the material tailoring, in which the required material properties can be obtained by manipulating the microstructure.

With the development of the finite element method (FEM) for problems governed by partial differential equations (*e.g.* mechanical, thermal, electrical, magnetic problems), the numerical simulation of heterogeneous systems can be directly

University of Liege
Computational & Multiscale Mechanics of Materials
Allée de la découverte 9, B4000 Liege, Belgium
Tel.: +32-4-366 48 26
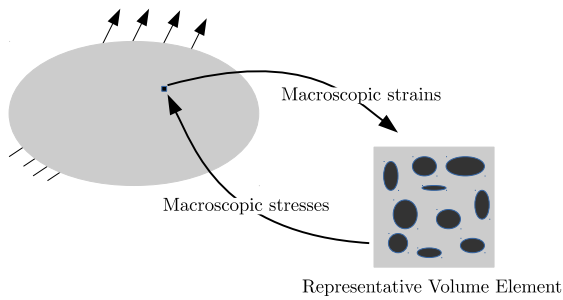E-mail: {vandung.nguyen, l.wu, l.noels}@ulg.ac.be

Fig. 1 Multi-scale computational homogenization strategy for heterogeneous materials

carried out by considering all local heterogeneities. However, if the characteristic size of the heterogeneities is much smaller than the structure dimensions, the calculation could not be performed since an enormous numerical system arises. An effective remedy, known as computational homogenization method (so-called FE^2), was pioneered in [1–5] to predict the effective properties of a material possessing complex microstructures, see also the review in [6] for more details. The basic idea of the FE^2 is to obtain macroscopic constitutive relations from the resolution of a microscopic boundary value problem (BVP) defined on a representative volume element (RVE) with an appropriate boundary condition as sketched out in Fig. 1. This technique does not result in the macroscopic constitutive relations in a closed form but they are always available through the resolution of the microscopic BVPs.

The FE^2 method was mainly applied to mechanical problems, see references [1–5, 7–14] as a non-exhausted list. This technique has also received the attention from other applications including purely thermal problems [15, 16], thermo-mechanical problems [17–19], electro-mechanical problems [20–22], magneto-mechanical problems [23], electro-magneto-mechanical problems [24, 25]. The FE^2 strategy relies on the principle of the separation of scales [6] which leads to assume that the microscopic BVP can be considered in a steady-state and can be formulated in a conventional form for mechanical, thermal, electrical, and magnetic parts. The evolution of the different physical fields (mechanical, thermal, electrical, *etc*) at the microscopic level is considered on a RVE, whose characteristic size is small with respect to the characteristic length of the macro-scale loading, but is large enough compared to the heterogeneities size so that all essential information of the underlying microstructure is provided in a statistically representative way [9, 26–28]. The resolution of an RVE associated to a macroscopic material point can be seen as a model of the material microstructure: the underlying microscopic BVP acts as a "virtual test" allowing the homogenized material behavior to be estimated. Therefore, the definition of the RVEs affects the accuracy in the modeling of the heterogeneous materials. In case of microstructure periodicity, the RVE can consist in one or several periodically repeated patterns as it contains all the necessary information. However, a real material is generally more complex and consists of different constituents which are randomly distributed. In this case, the RVEs can be constructed from micro-structural images using either the direct image processing [29, 30] or from the microstructure reconstruction [31, 32]. In general, the homogenized properties are shown to approach the effective values when increasing the RVE size with a rate which depends not only on the nature of the underlying

microstructure (properties of constituents, their distribution, and their interaction), but also on the proper choice of the microscopic boundary conditions [26]. Besides being used to extract bulk effective properties, the RVEs can be considered to study damage and failure, in which case their representativeness is also linked to the objectivity of the strength, fracture toughness, and traction-displacement jump softening response [33–37]. As the computation time increases with the RVE size, it is important to provide a critical size of the RVE allowing to capture the homogenized behavior at a reasonable computational cost [9, 26, 28]. However lack of representativeness of the volume element can also be exploited in order to study the material uncertainties on Statistical Volume Elements (SVEs) [38, 27], allowing defining meso-scale random fields [39–45], or propagating material uncertainties to the structural behavior [40, 46–48].

In the context of the kinematically admissible FEM, the FE^2 framework requires *a priori* an appropriate microscopic boundary condition, in which the macro-micro transition (downscaling) is constrained by the macroscopic kinematic variables. During the micro-macro transition (upscaling), the macroscopic quantities are evaluated by satisfying the energy consistency statements. Three conventional boundary condition types, *i.e.* the linear displacement boundary condition (LDBC), the minimal kinematic boundary condition (MKBC), and the periodic boundary condition (PBC), are often used [9, 7, 49, 12]. Other possibilities are available in the literature: *e.g.* the interpolation-based periodic boundary conditions (IPBC) [50], which are able to enforce the PBC in a general mesh setting and surf kinematically from the LDBC to the PBC when the interpolation degree increases; and the mixed boundary conditions (MBC) which combine different kinematic boundary conditions (LDBC, PBC, IPBC, and MKBC) on different parts of the RVE boundary. In the MBC category, the hybrid periodic boundary condition (HPBC) considered in [51, 52, 34] is a combination of the LDBC and the PBC; the orthogonal uniform mixed boundary conditions (OUMBC) combines the LDBC and MKBC in each facet of the RVE boundary as discussed in [53, 54, 47]; a broad range of allowable mixed boundary conditions inspired from using the Irving-Kirkwood procedure were considered [55]. The choice of the microscopic boundary condition affects numerical results not only in the homogenized constitutive behavior [9, 56] but also on the type and extend of damage taking place at the microscale [56]. The use of LDBC implies that the field at the RVE boundary is only controlled by a mapping of the macroscopic kinematic variables and results in a upper bound of the homogenized stiffness. The lower bound is obtained with the MKBC since the macroscopic kinematic variables are enforced at the microscale in the weakest sense [49]. For a given RVE size, the PBC provides in general a better estimation of the homogenized stiffness for both periodic and random microstructures [9]. The PBC naturally simulates the constraining effect of the surrounding material, although that constraint is in default when the microstructure is not periodic [56]. When considering microscopic problems with damage, the LDBC is too restrictive and suppresses the propagation of the localization band at the RVE boundary. The PBC results in a RVE deformed shape compatible with the periodic assumption of single or multiple localization bands. These nonphysical results can be avoided by using either the MKBC [49, 56], the OUMBC [36], or by using "Percolation Path Aligned Boundary Conditions (PPABC)" [35]. Although these mentioned boundary conditions were first considered in mechanical problems in which the displacement is the unknown field, their application to other unknown

fields in multi-physics problems is not limited, see [17,25, *e.g.*]. This work focuses on the unified treatment of these boundary conditions (at the exception of the PPABC type) in a multi-physics microscopic BVP.

Once the microscopic boundary conditions defined, the finite element discretization of the microscopic BVP is completed by a system of multiple-point linear constraints. To treat these multi-point constraints, two approaches are commonly used: (i) the direct constraint elimination; and (ii) the Lagrange multiplier method. The direct constraint elimination method allows reducing the total number of degrees of freedom of the microscopic BVP, see [4,12, *e.g.*]. However its computational procedure depends on the microscopic boundary condition type. The second approach consists in formulating the microscopic BVP using Lagrange multipliers to treat the multiple-point linear constraints arising from the microscopic boundary condition in a unified way. The resolution of the microscopic BVP can then be achieved using either the static multiplier condensation approach [8], the multiplier elimination approach [57], or the combined approach in which both the displacement unknowns and Lagrange multipliers are considered as total unknowns of the problems [58]. The static multiplier condensation approach requires the estimation of the Schur complements of the boundary nodes b in terms of the internal nodes i (under the matrix form $\tilde{\mathbf{K}}^{bb} = \mathbf{K}^{bb} - \mathbf{K}^{bi}\mathbf{K}^{ii-1}\mathbf{K}^{ib}$), which is costly in terms of both the computational time and the allocated memory in general and should be avoided. The use of the combined approach alters the positive definitive nature of the structural stiffness matrix with the saddle equilibrium point and increases the number of unknowns of the microscopic BVP. The multiplier elimination procedure following [57] allows a unified multiple constraint treatment and has been successfully applied to enforce microscopic boundary conditions as demonstrated in [11,13,59]. In comparison with the direct constraint elimination method, the multiplier elimination method allows formulating the microscopic BVP in a path following strategy for problems involving instabilities [13]. Herein, the treatment of the microscopic BVP is considered by both direct constraint elimination and Lagrange multiplier elimination approaches.

When considering a two-scale problem with a nested iterative resolution, the microscopic BVP at each integration point can be viewed as a "numerical material law", which provides the homogenized stresses and tangent operators of the homogenized behavior, see [10,34], or the microscopic BVP resolution can be directly coupled with the iterative resolution of the macroscopic BVP [60]. The first approach is adopted herein because the resolution of a large multi-scale problem can be easily handled in parallel using the ghost finite elements based on the Discontinuous Galerkin method [13]. Moreover, we will develop a method allowing the macroscopic tangent operators to be evaluated at a reduced computational time without the need of estimating Schur complements, while the coupled microscopic/macroscopic BVP resolution [60] requires this Schur complement evaluation, which is computationally expensive and requires a high memory storage.

When performing the two-scale simulations, the macroscopic stresses and macroscopic tangent operators of the homogenized behavior are required at every macroscopic integration points. As the explicit forms of these macroscopic data do not exist, they have to be numerically estimated from the finite element resolutions of the microscopic BVPs. From the generalized energy consistency condition between macroscopic and microscopic problems, the macroscopic stresses can be easily computed either from the volumetric averaging integrals of the microscopic

counterparts or from interface integrals based on the microscopic internal forces at the boundary nodes. The macroscopic tangent operators follow often either (i) from a numerical differentiation of the variations of the macroscopic stresses by applying variations on the macroscopic strains as suggested by [61], or (ii) from a stiffness condensation of the local microscopic stiffness matrix at the equilibrium state. The first approach is often considered for linear problems in which different deformation modes are separately applied to the microscopic problem and the macroscopic tangent operators directly result from the homogenized stresses [11, 50]. For problems involving nonlinearities, the resolution procedure of the microscopic BVP is reapplied for each perturbed macroscopic strain tensors but the computation time increases with the dimension of the macroscopic strain tensors (*e.g.* from 9 in first-order mechanical homogenization to 36 in a second-order mechanical homogenization). The second approach can be achieved in combination with the Lagrange multiplier method [8] or by performing a static condensation procedure [7,17,19, *e.g.*]. With the methods based on the stiffness condensation, the stiffness matrix needs to be partitioned, and dense matrices based on the Schur complements need to be estimated. These operations can be very time-consuming and require a lot of memory depending on the number of degrees of freedom of the problems. This work proposes an efficient method based on the linearization of the governing equations at the converged solution of the microscopic BVP (so-called in-system approach), allowing the macroscopic tangent operators to be computed without a significant effort.

The main contribution of the present work is twofold. On the one hand, although computational homogenization schemes are largely described in the literature, the numerical treatments of the constrained micro-scale BVP and of its boundary condition are often specialized to the physics and problem nature under consideration. In the work, we propose a unified micro-scale boundary value problem formulation for multi-physics problems in which an arbitrary number of extra-fields can be considered besides the mechanical field. As a result a library of constraint elements is available and allows constructing different kind of microscopic boundary conditions. On the other hand, we propose an original resolution of the constrained microscale BVP –for any kind of ("consistent") microscopic boundary condition– which yields the macroscopic tangent operators without requiring the evaluation of Schur complements, contrarily to the usually considered formulations. This resolution can be based either on the constraints elimination method or on the Lagrange multiplier elimination method, in which case it can be seen as an extension of the methodology developed in [57] to homogenization. The macroscopic tangent operators are computed from the linear system of the microscopic stiffness matrix, which does not need to be partitioned, with multiple right hand sides. Moreover, as the resolution of the linearized system of the microscopic BVP often follows a direct factorization procedure (*e.g.* LU factorization), the estimation of the macroscopic tangent operators is then performed with this factorized matrix so that the required computational time is much smaller than the one required to solve the linearized system of the microscopic BVP. As a result the concurrent multi-scale method gains in computational efficiency and in memory requirement as the macroscopic tangent operator is evaluated at a negligible cost.

The paper is organized as follows. The general strong form for a multi-physics BVP is summarized in Section 2. The unified finite element resolutions based on the

constraint elimination and Lagrange multiplier elimination procedures are detailed in Section 3, in which the explicit expressions of the macroscopic quantities are provided. Several numerical applications, such as first-order mechanical, thermal, and second-order mechanical homogenizations, and a thermo-mechanical two-scale problem are considered in Section 4 to demonstrate the efficiency of the proposed unified framework.

2 Microscopic multi-physics boundary value problem

Different possibilities have been used to formulate the FE^2 for mechanical problems such as the first-order, second-order, continuous-discontinuous homogenizations, see the review [6] and references therein. Although macroscopic formulations can vary depending on the nature of the macroscopic problems (*e.g.* classical Cauchy, Mindlin strain gradient, enriched-discontinuity continua, respectively for first-order, second-order, and continuous-discontinuous homogenizations), the microscopic BVPs are normally formulated in terms of the classical continuum mechanics. The required constitutive relations at the macro-scale are obtained from the resolution of the microscopic BVP through the scale transition between the macroscopic and microscopic problems. Apart from mechanics, the microscopic BVP can also deal with other physical phenomena (*e.g.* thermal, electrical, and magnetic ingredients), and the microscopic BVP should thus be formulated in terms of multiple physical fields, leading to a corresponding microscopic multi-physics BVP. By assuming the principle of separation of scales, these phenomena are governed by the conventional steady balance laws. The governing equations of the microscopic multi-physics BVP are summarized in this section.

2.1 General strong form

Considering a RVE whose reference configuration is denoted by V_0 and whose boundary is denoted by ∂V_0, the deformed configuration is characterized by a two-point mapping $\mathbf{x}_m = \mathbf{x}_m(\mathbf{X}_m)$, where $\mathbf{x}_m$ and $\mathbf{X}_m$ denote respectively the current and the reference positions of a material point in V_0. The deformation gradient $\mathbf{F}_m$ is defined at that point by

$$\mathbf{F}_m = \mathbf{x}_m \otimes \boldsymbol{\nabla}_0 \,, \tag{1}$$

where $\boldsymbol{\nabla}_0$ is the gradient operator with respect to the reference coordinates. In terms of the first Piola-Kirchhoff stress $\mathbf{P}_m$, which is energetically conjugated with $\mathbf{F}_m$, the local mechanical equilibrium state is governed by

$$\mathbf{P}_m \cdot \boldsymbol{\nabla}_0 = \mathbf{0} \text{ on } V_0 \,, \tag{2}$$

in the absence of body forces.

Apart from the mechanical field, the microscopic BVP is assumed to combine some other scalar fields (*e.g.* thermal, electrical, magnetic fields), so-called extra-fields and denoted by θ_m^k with $k = 1, ..., N$ and N being the number of extra-fields. Similarity to the mechanical part, the extra-field gradients are given by

$$\boldsymbol{\varphi}_m^k = \boldsymbol{\nabla}_0 \theta_m^k \text{ with } k = 1, ..., N \,. \tag{3}$$

The extra-field fluxes $\boldsymbol{\mathcal{T}}_m^k$ with $k = 1, ..., N$ are defined as conjugate quantities with $\boldsymbol{\varphi}_m^k$ respectively. Depending on the nature of θ_m^k, such as temperature, electric potential, or magnetic potential, one has respectively the heat flux vector, electrical displacement vector, or magnetic flux density vector. The steady balance laws governing the extra-fields read

$$\boldsymbol{\nabla}_0 \cdot \boldsymbol{\mathcal{T}}_m^k = 0 \text{ on } V_0 \text{ for } k = 1, ..., N , \tag{4}$$

as considered in thermal problems [15], electrical, and magnetic problems [25].

In the FE^2 technique, the constitutive relations at the micro-scale are given under the fully-coupled forms

$$\begin{cases} \mathbf{P}_m = \mathbf{P}_m \left(\mathbf{F}_m, \theta_m^1, \boldsymbol{\varphi}_m^1, ..., \theta_m^N, \boldsymbol{\varphi}_m^N; \mathbf{Z} \right) \\ \boldsymbol{\mathcal{T}}_m^k = \boldsymbol{\mathcal{T}}_m^k \left(\mathbf{F}_m, \theta_m^1, \boldsymbol{\varphi}_m^1, ..., \theta_m^N, \boldsymbol{\varphi}_m^N; \mathbf{Z} \right) \end{cases} \quad \text{with } k = 1, ..., N , \tag{5}$$

where $\mathbf{Z}$ is a vector including all historic-dependent internal variables in order to follow the historic-dependent processes. Eq. (5) represents fully-coupled constitutive relations. The microscopic boundary condition needs to be specified to close the formulation statement of the microscopic problem following the macro-micro transition as detailed in the next section.

Since the mechanical and extra-field governing equations following Eqs. (2, 4) are similar to each other, a generalized representation is introduced. The microscopic generalized position $\boldsymbol{\mathcal{X}}_m$ is defined by including all microscopic primary variables over V_0 as

$$\boldsymbol{\mathcal{X}}_m = \left[\mathbf{x}_m^T \ \theta_m^1 \ ... \ \theta_m^N \right]^T . \tag{6}$$

The dimension of $\boldsymbol{\mathcal{X}}_m$ is $d + N$, where d is the dimension of the mechanical problems. This work develops the methodology for $d = 3$ as a general case. The generalized position can be divided into two parts: (i) $\boldsymbol{\mathcal{X}}_m^{NC}$ consists of components, which do not appear explicitly in the constitutive relations (e.g. position, electrical potential, or magnetic potential), and (ii) $\boldsymbol{\mathcal{X}}_m^C$ includes all remaining components, which participate explicitly to the constitutive laws (e.g. temperature). From the definition of the generalized position in Eq. (6), the microscopic generalized strain and microscopic generalized stress can be defined respectively by

$$\boldsymbol{\mathcal{F}}_m = \left[\mathbf{F}_m^T \ \boldsymbol{\varphi}_m^1 \ ... \ \boldsymbol{\varphi}_m^N \right]^T , \text{and} \tag{7}$$

$$\boldsymbol{\mathcal{P}}_m = \left[\mathbf{P}_m^T \ \boldsymbol{\mathcal{T}}_m^1 \ ... \ \boldsymbol{\mathcal{T}}_m^N \right]^T . \tag{8}$$

Considering an arbitrary generalized tensor $\boldsymbol{\mathcal{A}} = \left[\mathbf{A}_1^T \ \mathbf{A}_2^T \ ... \ \mathbf{A}_N^T \right]^T$, an arbitrary generalized tensor $\boldsymbol{\mathcal{B}} = \left[\mathbf{B}_1^T \ \mathbf{B}_2^T \ ... \ \mathbf{B}_N^T \right]^T$ and an arbitrary tensor $\mathbf{C}$, one can define an arbitrary tensorial operator $\bullet$

$$\boldsymbol{\mathcal{A}} \bullet \boldsymbol{\mathcal{B}} = \begin{bmatrix} \mathbf{A}_1 \bullet \mathbf{B}_1 \\ \mathbf{A}_2 \bullet \mathbf{B}_2 \\ \vdots \\ \mathbf{A}_N \bullet \mathbf{B}_N \end{bmatrix} , \boldsymbol{\mathcal{A}} \bullet \mathbf{C} = \begin{bmatrix} \mathbf{A}_1 \bullet \mathbf{C} \\ \mathbf{A}_2 \bullet \mathbf{C} \\ \vdots \\ \mathbf{A}_N \bullet \mathbf{C} \end{bmatrix} , \text{ and } \mathbf{C} \bullet \boldsymbol{\mathcal{A}} = \begin{bmatrix} \mathbf{C} \bullet \mathbf{A}_1 \\ \mathbf{C} \bullet \mathbf{A}_2 \\ \vdots \\ \mathbf{C} \bullet \mathbf{A}_N \end{bmatrix} . \tag{9}$$

Using the generalized representation, the strong forms (2, 4) are rewritten as

$$\boldsymbol{\mathcal{P}}_m \cdot \boldsymbol{\nabla}_0 = \mathbf{0} \text{ on } V_0 \,. \tag{10}$$

The microscopic generalized strain can be rewritten from Eq. (7) as

$$\boldsymbol{\mathcal{F}}_m = \boldsymbol{\mathcal{X}}_m \otimes \boldsymbol{\nabla}_0 \,. \tag{11}$$

As $\boldsymbol{\mathcal{X}}_m^{NC}$ does not participate explicitly to the constitutive relations, Eq. (5) can be rewritten in the generalized representation as

$$\boldsymbol{\mathcal{P}}_m = \boldsymbol{\mathcal{P}}_m \left(\boldsymbol{\mathcal{X}}_m^C, \boldsymbol{\mathcal{F}}_m; \mathbf{Z} \right) \,. \tag{12}$$

The microscopic generalized tangent operators are defined from Eq. (12) yielding

$$\boldsymbol{\mathcal{L}}_m = \frac{\partial \boldsymbol{\mathcal{P}}_m}{\partial \boldsymbol{\mathcal{F}}_m} \,, \text{ and } \boldsymbol{\mathcal{J}}_m = \frac{\partial \boldsymbol{\mathcal{P}}_m}{\partial \boldsymbol{\mathcal{X}}_m^C} \,. \tag{13}$$

The macroscopic quantities $\boldsymbol{\mathcal{X}}_M$, $\boldsymbol{\mathcal{X}}_M^{NC}$, $\boldsymbol{\mathcal{X}}_M^C$, $\boldsymbol{\mathcal{F}}_M$, $\boldsymbol{\mathcal{P}}_M$, $\boldsymbol{\mathcal{L}}_M$, and $\boldsymbol{\mathcal{J}}_M$ are defined as counterparts of their respective microscopic quantities.

2.2 General microscopic boundary condition

The local equilibrium state over the RVE is commonly driven by the macroscopic kinematic variables by defining a microscopic boundary condition. Considering an arbitrary field[1] $\mathcal{X}_m^k$ of $\boldsymbol{\mathcal{X}}_m$, in order to downscale the related macroscopic kinematic variables to the microscopic BVP, its value at an arbitrary point $\mathbf{X}_m \in V_0$ can be decomposed as

$$\mathcal{X}_m^k = \Phi_m^k + \mathcal{W}_m^k \text{ on } V_0 \,, \tag{14}$$

where Φ_m^k is a truncated Taylor series around the RVE geometric center and $\mathcal{W}_m^k$ is the the microscopic fluctuation of the field $\mathcal{X}_m^k$, which represents the field fluctuation due to the microscopic heterogeneities. The expression of the truncated Taylor series Φ_m^k depends on the homogenization order as a function of the macroscopic kinematic quantities and of the local coordinates. In the context of the first-order homogenization

$$\Phi_m^k = \mathcal{X}_M^k + \boldsymbol{\mathcal{F}}_M^k \cdot \mathbf{X}_m \,, \tag{15}$$

and in the context of the second-order homogenization, a second-order term enhances Eq. (15), leading to

$$\Phi_m^k = \mathcal{X}_M^k + \boldsymbol{\mathcal{F}}_M^k \cdot \mathbf{X}_m + \frac{1}{2} \boldsymbol{\mathcal{G}}_M^k : (\mathbf{X}_m \otimes \mathbf{X}_m) \,. \tag{16}$$

In the last two equations, $\mathcal{X}_M^k$, $\boldsymbol{\mathcal{F}}_M^k$, and $\boldsymbol{\mathcal{G}}_M^k$ are the macroscopic quantities (field value, its gradient, and its second-order gradient) and $\mathbf{X}_m$ is the microscopic position in the coordinate system attached to the RVE geometric center satisfying $\int_{V_0} \mathbf{X}_m \, dV = \mathbf{0}$.

---

[1] The position vector $\mathbf{x}_m$ can be considered as three scalar components from which the deformation gradient $\mathbf{F}_m$ can be rewritten as a group of three vectors.

The macro-micro kinematic coupling is satisfied by assuming the equality of the volume average of the microscopic field gradient and the macroscopic counterpart [5, 7, 10] leading to

$$\int_{\partial V_0} \mathcal{W}_m^k \mathbf{N}_m \, dS = \mathbf{0} \,, \tag{17}$$

where $\mathbf{N}_m$ is the outward normal to the RVE boundary ∂V_0 in the reference configuration. In the case of the second-order homogenization, the following additional constraint

$$\int_{\partial V_0} \mathcal{W}_m^k \mathbf{N}_m \otimes \mathbf{X}_m \, dS = \mathbf{0} \,, \tag{18}$$

needs to be considered [10, 11] in order to enforce the second-order gradients at the micro-scale while remaining the microscopic BVP in the conventional continuum.

If the field value $\mathcal{X}_m^k$ appears explicitly in the microscopic constitutive relations ($\mathcal{X}_m^k$ in $\boldsymbol{\mathcal{X}}_m^C$), the enforcement of $\mathcal{X}_M^k$ to the microscopic BVP has to be considered. For this purpose, the field equivalence condition needs to be considered

$$\frac{1}{V_0} \int_{V_0} w_m^k \, dV = w_M^k \text{ if } \mathcal{X}_m^k \text{ in } \boldsymbol{\mathcal{X}}_m^C \,, \tag{19}$$

where w_m^k and w_M^k are the microscopic and macroscopic field capacity indicators, which are defined as functions of the field values $\mathcal{X}_m^k$ and $\mathcal{X}_M^k$, respectively. The explicit expressions of w_m^k and of w_M^k depend on the nature of $\mathcal{X}_m^k$ and on the problem statement. In a straightforward way, this condition can be formulated in terms of the field capacity equivalence by considering[2]

$$\begin{cases} w_m^k = C_m^k \mathcal{X}_m^k \\ w_M^k = C_M^k \mathcal{X}_M^k \end{cases} \,, \tag{20}$$

where C_m^k is the field capacity per unit of $\mathcal{X}_m^k$ and where C_M^k is its macroscopic counterpart which is given by

$$C_M^k = \frac{1}{V_0} \int_{V_0} C_m^k \, dV \,. \tag{21}$$

In problems involving temperature, the temperature transition can be enforced by the heat energy equivalence condition following Eq. (20) as considered in [15, 17]. As the group $\boldsymbol{\mathcal{X}}_m^{NC}$ does not explicitly participate to the constitutive relations, the condition (19) does not have to be considered for the fields belonging to $\boldsymbol{\mathcal{X}}_m^{NC}$ but additional conditions might have to be provided in order to prevent rigid body motion modes if necessary.

The kinematic constraints (17, 18, 19) are fundamental requirements of the macro-micro transition for each field $\mathcal{X}_m^k$. The separation of the macro-micro transition statement allows combining a first-order homogenization of one field with a second-order homogenization of another field. By considering a general three-dimensional parallelepiped RVE, its boundary ∂V_0 can be divided into 6 facets,

---

[2] In a general case, a nonlinear function can be considered, providing it is linearized at the current time step.

denoted by S^j with $j = 1, ..., 6$ so that S^i and S^{i+3} are opposite for $i = 1, 2, 3$. For each facet S^i, the outward normal is constant and denoted by $\mathbf{N}_m^i$. Clearly, one has $\mathbf{N}_m^i = -\mathbf{N}_m^{i+3}$, and Eq. (17) can be rewritten as

$$\int_{S^i} \mathcal{W}_m^k \, dS - \int_{S^{i+3}} \mathcal{W}_m^k \, dS = 0 \text{ with } i = 1, 2, 3 \,. \tag{22}$$

Similarly, Eq. (18) can be rewritten as

$$\int_{S^i} \mathcal{W}_m^k \mathbf{X}_m \, dS - \int_{S^{i+3}} \mathcal{W}_m^k \mathbf{X}_m \, dS = \mathbf{0} \text{ with } i = 1, 2, 3 \,. \tag{23}$$

Clearly, the kinematic constraints can be separately considered for each pair of facets (S^i, S^{i+3}). Some microscopic boundary conditions result naturally in satisfying *a priori* Eqs. (22, 23) as detailed in Section 3. The condition (19) has to be directly constrained as it is formulated on the whole RVE. Moreover, it prevents the rigid body motion mode of the field $\mathcal{X}_m^k$. In the following sections, only a parallelepiped RVE is considered.

2.3 Extraction of the macroscopic quantities

Considering an arbitrary field $\mathcal{X}_m^k$, the generalized Hill-Mandel condition results in the averaging relation of the macroscopic generalized stress and its microscopic counterpart [10,25],

$$\boldsymbol{\mathcal{P}}_M^k = \frac{1}{V_0} \int_{\partial V_0} \boldsymbol{\mathcal{P}}_m^k \, dV \,. \tag{24}$$

If the second-order homogenization is employed, the macroscopic generalized higher-order stress ($\boldsymbol{\mathcal{Q}}_M^k$) can be estimated by the following relation [10]

$$\boldsymbol{\mathcal{Q}}_M^k = \frac{1}{2V_0} \int_{\partial V_0} \boldsymbol{\mathcal{P}}_m^k \otimes \mathbf{X}_m + \mathbf{X}_m \otimes \boldsymbol{\mathcal{P}}_m^k \, dV \,. \tag{25}$$

The macroscopic generalized tangent operators defining the variations of the macroscopic generalized stress with respect to the variations of the macroscopic generalized strain and with respect to the variations of the generalized position participating to the constitutive laws are respectively estimated by

$$\boldsymbol{\mathcal{L}}_M = \frac{\partial \boldsymbol{\mathcal{P}}_M}{\partial \boldsymbol{\mathcal{F}}_M} \text{ and } \boldsymbol{\mathcal{J}}_M = \frac{\partial \boldsymbol{\mathcal{P}}_M}{\partial \boldsymbol{\mathcal{X}}_M^C} \,. \tag{26}$$

The computation of the generalized tangent operators cannot be obtained in a straightforward way from their microscopic counterparts ($\boldsymbol{\mathcal{L}}_m$ and $\boldsymbol{\mathcal{J}}_m$) since they are defined through partial derivatives of volumetric integrals.

Besides the generalized stresses, some microscopic fields (*e.g.* thermoelastic heating [19], average strain over active damage zone [34]), denoted by $\boldsymbol{\mathcal{Z}}_m$, need to be upscaled by a volumetric integral

$$\boldsymbol{\mathcal{Z}}_M = \frac{1}{V_0} \int_{V_0} \boldsymbol{\mathcal{Z}}_m \, dV \,. \tag{27}$$

Their related tangent operators need to be estimated by

$$\boldsymbol{\mathcal{Y}}_{\boldsymbol{\mathcal{F}}_M} = \frac{\partial \boldsymbol{\mathcal{Z}}_M}{\partial \boldsymbol{\mathcal{F}}_M} \text{ and } \boldsymbol{\mathcal{Y}}_{\boldsymbol{\mathcal{X}}_M^C} = \frac{\partial \boldsymbol{\mathcal{Z}}_M}{\partial \boldsymbol{\mathcal{X}}_M^C} . \tag{28}$$

Similarly to the computation of the generalized tangent operators in Eq. (26), the computation of $\boldsymbol{\mathcal{Y}}_{\boldsymbol{\mathcal{F}}_M}$ and $\boldsymbol{\mathcal{Y}}_{\boldsymbol{\mathcal{X}}_M^C}$ is not straightforwardly obtained from their microscopic counterparts $\boldsymbol{\mathcal{Y}}_{\boldsymbol{\mathcal{F}}_m}$ and $\boldsymbol{\mathcal{Y}}_{\boldsymbol{\mathcal{X}}_m^C}$, which are explicitly provided from the microscopic constitutive law.

2.4 Variational form of the microscopic boundary value problem

As a consequence of the generalized Hill-Mandel condition [12,25], the weak form of the microscopic BVP is stated as finding $\boldsymbol{\mathcal{W}}_m \in \boldsymbol{U}$ such that

$$\int_{V_0} \boldsymbol{\mathcal{P}}_m \odot (\delta \boldsymbol{\mathcal{W}}_m \otimes \boldsymbol{\nabla}_0) \, dV = \boldsymbol{0} \ \forall \delta \boldsymbol{\mathcal{W}}_m \in \boldsymbol{U} , \tag{29}$$

where $\odot$ is the scalar product operator defined with two n^{th} order tensors $\mathbf{A}$ and $\mathbf{B}$ by

$$\mathbf{A} \odot \mathbf{B} = A_{i_1 i_2 \dots i_n} B_{i_1 i_2 \dots i_n} , \tag{30}$$

and where the admissibility kinematic field $\boldsymbol{U}$ is defined from the kinematic function space U^k of each field $\mathcal{X}_m^k$ by

$$\boldsymbol{U} = \mathrm{U}^1 \times \mathrm{U}^2 \times \dots \times \mathrm{U}^{d+N} . \tag{31}$$

with U^k constructed following Eqs. (19, 22, 23). The weak form (29) is resolved by means of the finite element method (FEM) in Section 3.

3 Finite element resolution of the microscopic BVP

This section provides a unified finite element resolution of the weak form (29) within a non-linear finite element framework. The vector-matrix notations are used in this section instead of the tensor ones. A general rule allowing to convert an arbitrary tensor into its vector-matrix representation is provided in Appendix A. In the vector-matrix representation, Eq. (14) can be rewritten under a matrix form

$$\mathcal{U}_m^k = \mathbf{S}_m^k \boldsymbol{\mathcal{K}}_M^k + \mathcal{W}_m^k , \tag{32}$$

where $\mathcal{U}_m^k$ is the degree of freedom of the field $\mathcal{X}_m^k$ at $\mathbf{X}_m$ and given by

$$\mathcal{U}_m^k = \begin{cases} \mathcal{X}_m^k & \text{if } \mathcal{X}_m^k \in \boldsymbol{\mathcal{X}}_m^C \\ \mathcal{X}_m^k - \mathcal{X}_M^k & \text{if } \mathcal{X}_m^k \in \boldsymbol{\mathcal{X}}_m^{NC} \end{cases} , \tag{33}$$

where $\mathcal{K}_M^k$ is a vector including all macroscopic kinematic variables participating to the constitutive relations related to the field $\mathcal{X}_M^k$

$$\mathcal{K}_M^k = \begin{cases} \left[\mathcal{X}_M^k \ \ \mathcal{F}_M^{k\,T} \ \ \mathcal{G}_M^{k\,T} \ \ldots \right]^T & \text{if } \mathcal{X}_m^k \in \mathcal{X}_m^C \\ \left[\mathcal{F}_M^{k\,T} \ \ \mathcal{G}_M^{k\,T} \ \ldots \right]^T & \text{if } \mathcal{X}_m^k \in \mathcal{X}_m^{NC} \end{cases}, \tag{34}$$

and where $\mathbf{S}_m^k$ is the kinematic matrix depending only on the material coordinates at that point

$$\mathbf{S}_m^k \left(\mathbf{X}_m \right) = \begin{cases} \left[1 \ \ \mathbf{X}_m^T \ \ \frac{1}{2}\mathbf{X}_{sq}^T \ \ldots \right] & \text{if } \mathcal{X}_m^k \in \mathcal{X}_m^C \\ \left[\mathbf{X}_m^T \ \ \frac{1}{2}\mathbf{X}_{sq}^T \ \ldots \right] & \text{if } \mathcal{X}_m^k \in \mathcal{X}_m^{NC} \end{cases}. \tag{35}$$

In the last equation $\mathbf{X}_{sq} = \text{vec} \left(\mathbf{X}_m \otimes \mathbf{X}_m \right)$. Following Eq. (32), the unknown fields are defined as functions of the macroscopic kinematic variables and of the microscopic fluctuations.

The RVE V_0 is discretized into finite elements such that $V_0 = \bigcup_e V_0^e$. The kinematic constraints resulting from the microscopic boundary conditions described in Section 2 have to be applied on the finite element mesh of the RVE boundary. The test and trial functions are defined over an element V_0^e in terms of the standard interpolation concept

$$\begin{cases} \mathcal{U}_m \left(\mathbf{X}_m \right) & = \mathbf{N}^e \left(\mathbf{X}_m \right) \left[\mathcal{U}_m \right]_{V_0^e} \\ \delta \mathcal{W}_m \left(\mathbf{X}_m \right) & = \mathbf{N}^e \left(\mathbf{X}_m \right) \left[\delta \mathcal{W}_m \right]_{V_0^e} \end{cases} \text{ over } V_0^e, \tag{36}$$

where $\mathcal{U}_m$ denotes the unknown fields at $\mathbf{X}_m$, where $\mathbf{N}^e$ is a matrix consisting of the shape functions, and where $[\bullet]_{V_0^e}$ defines a vector over V_0^e by collecting the nodal quantity $\bullet$.

3.1 Treatment of the microscopic boundary condition

With the finite element discretization of the RVE, the microscopic boundary condition leads to a muti-point linear constraints system, from which the resolution procedure of the microscopic BVP depends on the microscopic boundary condition type [8,12]. Owing to the diversity of microscopic boundary condition kinds, it is necessary to provide an unified strategy for the constraints treatment. For that purpose, this work follows a strategy based on the constraint elements. A library of constraint elements is first created based on the basic microscopic boundary conditions (LDBC, MKBC, PBC, *etc.*). Then the muti-point linear constraints system arising from a proper microscopic boundary condition can be represented by a group of suitable constraint elements from the library. This strategy provides an efficient way allowing, not only to easily manage the multi-point constraints resulting from the microscopic boundary condition, but also to apply their unified treatment. A mixed boundary condition can be easily generated using this library. A typical constraint element e possesses a general form

$$\mathbf{C}_e \mathcal{U}_e - \mathbf{S}_e \mathcal{K}_M^k = 0, \tag{37}$$

where $\mathbf{C}_e$ is the elementary constraint matrix, $\boldsymbol{\mathcal{U}}_e$ is a vector containing all the related unknowns of the field $\mathcal{X}_m^k$, $\mathbf{S}_e$ is the elementary kinematic matrix. Some typical constraint elements and their matrices $\mathbf{C}_e$, $\mathbf{S}_e$, $\boldsymbol{\mathcal{U}}_e$, which depend on the microscopic boundary condition type, are described in the following.

3.1.1 Zero fluctuation constraint element

The conditions (22) and (23) can be trivially satisfied using the zero fluctuation boundary condition (ZFBC)

$$\mathcal{W}_m^k = 0 \text{ on } S^i \cup S^{i+3}\,. \tag{38}$$

The term "linear displacement boundary condition (LDBC)" is often used to call this boundary condition type when considering the first-order homogenization.

On an arbitrary mesh node $\mathbf{X}_m$ satisfying Eq. (38), Eq. (32) leads to

$$\mathcal{U}_m^k = \mathbf{S}_m^k \boldsymbol{\mathcal{K}}_M^k\,. \tag{39}$$

The constrained elementary matrices following Eq. (37) can be expressed by

$$\boldsymbol{\mathcal{U}}_e = \left[\mathcal{U}_m^k\right]\,, \mathbf{C}_e = \begin{bmatrix}1\end{bmatrix}\,, \text{ and } \mathbf{S}_e = \mathbf{S}_m^k\,, \tag{40}$$

where $\mathbf{S}_m^k$ is given in Eq. (35).

3.1.2 Zero average fluctuation constraint element

This constraint element comes from the minimal kinematic boundary condition (MKBC) by directly satisfying Eq. (22) using stronger conditions

$$\int_{S^i} \mathcal{W}_m^k \, dS = \int_{S^{i+3}} \mathcal{W}_m^k \, dS = 0\,. \tag{41}$$

This kind of constraints leads to consider a general form

$$\int_S \mathbb{W}\left(\mathbf{X}_m\right) \mathcal{W}_m^k \, dS = 0\,, \tag{42}$$

where $\mathbb{W}$ is the weight function defined as a function of $\mathbf{X}_m$ and $S = \bigcup_e S^e$ is an arbitrary surface finite elements group. The kinematic constraints following Eqs. (41) can be obtained by particularizing $\mathbb{W} = 1$.

Using Eq. (32), Eq. (42) can be rewritten as

$$\frac{1}{S} \int_S \mathbb{W}\left(\mathbf{X}_m\right) \mathcal{U}_m^k \, dS - \frac{1}{S} \left(\int_S \mathbb{W}\left(\mathbf{X}_m\right) \mathbf{S}_m^k \, dS\right) \boldsymbol{\mathcal{K}}_M^k = 0\,. \tag{43}$$

Following the finite element discretization $S = \bigcup_e S^e$, the elementary unknowns vector is given by

$$\boldsymbol{\mathcal{U}}_e = \left[\mathcal{U}_m^k\right]_S\,, \tag{44}$$

where $\left[\mathcal{U}_m^k\right]_S$ consists of all unknowns from the mesh nodes over S. The standard interpolation concept applies for each element S^e so that

$$\frac{1}{S} \int_S \mathbb{W} \mathcal{U}_m^k \, dS = \frac{1}{S} \sum_{S^e \in S} \int_{S^e} \mathbb{W} \mathbb{N}^e \, dS \left[\mathcal{U}_m^k\right]_{S^e} = \mathbf{C}_e \boldsymbol{\mathcal{U}}_e \, , \tag{45}$$

where $\mathbb{N}^e$ is the matrix of shape functions over the element S^e. Using Eqs. (44, 45), the elementary constraint matrices following Eq. (37) are given by

$$\mathbf{C}_e = \bigwedge_{S^e \in S} \left(\frac{1}{S} \int_{S^e} \mathbb{W} \mathbb{N}^e \, dS \right) \, , \text{ and} \tag{46}$$

$$\mathbf{S}_e = \frac{1}{S} \int_S \mathbb{W} \mathbf{S}_m^k \, dS \, , \tag{47}$$

where $\bigwedge_{S^e \in S}$ is the assembly operator over S and where $\mathbf{S}_m^k$ is given in Eq. (35).

3.1.3 Periodic average fluctuation constraint element

This constraint element comes from the minimal kinematic boundary condition (MKBC) by directly satisfying Eqs. (22, 23). These constraints lead to consider an arbitrary pair of facets (S_1, S_2), the periodic condition of the average fluctuation is formulated by

$$\frac{1}{S_1} \int_{S_1} \mathbb{W}^1 \left(\mathbf{X}_m\right) \mathcal{W}_m^k \, dS - \frac{1}{S_2} \int_{S_2} \mathbb{W}^2 \left(\mathbf{X}_m\right) \mathcal{W}_m^k \, dS = 0 \, , \tag{48}$$

where $\mathbb{W}^1$ and $\mathbb{W}^2$ are respectively the weight functions on S_1 and S_2. The kinematic constraints following Eqs. (22, 23) can be obtained using $\mathbb{W}^1 = \mathbb{W}^2 = 1$ and $\mathbb{W}^1 = \mathbb{W}^2 = \mathbf{X}_m$ respectively.

Using Eq. (32), Eq. (48) can be rewritten as

$$\frac{1}{S_1} \int_{S_1} \mathbb{W}^1 \mathcal{U}_m^k \, , dS - \frac{1}{S_2} \int_{S_2} \mathbb{W}^2 \mathcal{U}_m^k \, , dS$$
$$- \left(\frac{1}{S_1} \int_{S_1} \mathbb{W}^1 \mathbf{S}_m^k \, dS - \frac{1}{S_2} \int_{S_2} \mathbb{W}^2 \mathbf{S}_m^k \, dS \right) \boldsymbol{\mathcal{K}}_M^k = 0 \, . \tag{49}$$

Following Eq. (37) one has

$$\boldsymbol{\mathcal{U}}_e = \begin{bmatrix} \boldsymbol{\mathcal{U}}_{e\,\text{MKBC}}\left(S_1\right) \\ \boldsymbol{\mathcal{U}}_{e\,\text{MKBC}}\left(S_2\right) \end{bmatrix} \, , \mathbf{C}_e = \begin{bmatrix} \mathbf{C}_{e\,\text{MKBC}}\left(S_1\right) & -\mathbf{C}_{e\,\text{MKBC}}\left(S_2\right) \end{bmatrix} \, , \text{ and} \tag{50}$$

$$\mathbf{S}_e = \mathbf{S}_{e\,\text{MKBC}}\left(S_1\right) - \mathbf{S}_{e\,\text{MKBC}}\left(S_2\right) \, , \tag{51}$$

where $\boldsymbol{\mathcal{U}}_{e\,\text{MKBC}}$, $\mathbf{C}_{e\,\text{MKBC}}$, and $\mathbf{S}_{e\,\text{MKBC}}$ are given in Eqs. (44, 46, 47), respectively.

3.1.4 Periodic fluctuation constraint element

This constraint element comes from the periodic boundary condition (PBC). Eq. (22) can be satisfied if the fluctuation periodicity is stated

$$\mathcal{W}_m^k \left(\mathbf{X}_m^+ \right) - \mathcal{W}_m^k \left(\mathbf{X}_m^- \right) = \mathbf{0} \,, \tag{52}$$

where $\left(\mathbf{X}_m^+, \mathbf{X}_m^- \right) \in \left(S^i, S^{i+3} \right)$ is matching nodes. Using Eq. (32), one has

$$\mathcal{U}_m^k \left(\mathbf{X}_m^+ \right) - \mathcal{U}_m^k \left(\mathbf{X}_m^- \right) - \left[\mathbf{S}_m^k \left(\mathbf{X}_m^+ \right) - \mathbf{S}_m^k \left(\mathbf{X}_m^- \right) \right] \mathcal{K}_M^k = 0 \,. \tag{53}$$

Following Eq. (37) one has

$$\boldsymbol{\mathcal{U}}_e = \begin{bmatrix} \mathcal{U}_m^k \left(\mathbf{X}_m^+ \right) \\ \mathcal{U}_m^k \left(\mathbf{X}_m^- \right) \end{bmatrix} \,, \mathbf{C}_e = \begin{bmatrix} 1 & -1 \end{bmatrix} \,, \text{and } \mathbf{S}_e = \mathbf{S}_m^k \left(\mathbf{X}_m^+ \right) - \mathbf{S}_m^k \left(\mathbf{X}_m^- \right) \,, \tag{54}$$

where $\mathbf{S}_m^k$ is given in Eq. (35).

3.1.5 Interpolation-based periodic fluctuation constraint element

In a general mesh setting, the matching node condition can not always be satisfied. For this mesh type, applying the first-order or the second-order PBCs is not trivial. This has motivated the development of the interpolation-based periodic boundary condition (IPBC) in both the first-order homogenization [50] and the second-order homogenization [13]. In this case, interpolation forms are introduced to approximate the PBC. By considering a pair of facets (S^i, S^{i+3}) satisfying the PBC, one can defined an interpolation form

$$\mathbb{S}^i = \sum_{k=1}^{n+1} \mathbb{N}_k^i \left(\mathbf{X}_m \right) a_k^i \text{ (no sum on } i) \,, \tag{55}$$

where n is the interpolation degree, $\mathbb{N}_k^i$ with $k = 1, ..., n+1$ are the interpolation shape functions, and a_k^i with $k = 1, ..., n+1$ are additional degrees of freedom. The IPBC is naturally obtained by enforcing

$$\begin{cases} \mathcal{W}_m^k \left(\mathbf{X}_m^+ \right) & = \mathbb{S}^i \left(\mathbf{X}_m^- \right) \, \forall \mathbf{X}_m^+ \in S^{i+3} \\ \mathcal{W}_m^k \left(\mathbf{X}_m^- \right) & = \mathbb{S}^i \left(\mathbf{X}_m^- \right) \, \forall \mathbf{X}_m^- \in S^i \,. \end{cases} \tag{56}$$

This microscopic boundary condition can be applied on a general mesh setting. The ZFBC can be considered as a special case of the IPBC with a linear interpolation.

Considering an arbitrary mesh node $\mathbf{X}_m$ on the RVE boundary ∂V_0, the interpolation-based constraint element following the interpolation form (55) is given by

$$\mathcal{W}_m^k \left(\mathbf{X}_m \right) = \mathbb{S}^i \left(\mathbf{X}_m, a_1^i, \ldots, a_{n+1}^i \right) = \mathbf{A} \boldsymbol{\mathcal{U}}^I \,, \tag{57}$$

where a_j^i with $j = 1, ..., n+1$ are the additional unknowns, where

$$\boldsymbol{\mathcal{U}}^I = \begin{bmatrix} a_1^i & a_2^i & \ldots & a_{n+1}^i \end{bmatrix}^T \,, \tag{58}$$

is a vector containing all additional degrees of freedom used in the interpolation form $\mathbb{S}^i$, and where $\mathbf{A}$ is the constraint coefficients matrix constructed from the values of the interpolation bases at $\mathbf{X}_m$. By switching the fluctuation $\mathcal{W}_m^k$ to the unknown with Eq. (32), Eq. (57) becomes

$$\mathcal{U}_m^k - \mathbf{S}_m^k \mathcal{K}_M^k - \mathbf{A}\mathcal{U}^I = \mathbf{0}\,. \tag{59}$$

The matrix components following Eq. (37) of this kind of constraint element are given by

$$\boldsymbol{\mathcal{U}}_e = \begin{bmatrix} \mathcal{U}_m^k \\ \boldsymbol{\mathcal{U}}^I \end{bmatrix},\, \mathbf{C}_e = \begin{bmatrix} 1 & -\mathbf{A} \end{bmatrix}\, ,\, \text{and } \mathbf{S}_e = \mathbf{S}_m^k\,, \tag{60}$$

where $\mathbf{S}_m^k$ is given in Eq. (35).

The matrix $\mathbf{A}$ at a boundary point $\mathbf{X}_m$ depends on the interpolation method. Theoretically, an arbitrary interpolation form can be considered. A simple interpolation form is suggested in [62] to enforce the PBC in a two-dimensional periodic RVE by enforcing a linear displacement field at intersections of fibers with RVE sides and a cubic displacement field at intersections of matrix with RVE sides. This work was later enhanced in [50] with an arbitrary interpolation form. In that work, the Lagrange and cubic spline interpolants were considered to demonstrate the implementation framework in 2-dimensional problems. From 2-dimensional interpolation formulations, the application on 3-dimensional cases can be easily derived using a bilinear patch Coons formulation. The finite element-based interpolation formulation, resulting in the so-called quasi-periodic boundary condition, was considered to apply the periodic boundary condition on a foamed RVE [63]. Finally, the master/slave approach [64] can be considered as a special case of finite element-based interpolation by considering directly the finite element mesh at the RVE boundary as interpolation bases.

3.1.6 Field equivalence constraint element

This constraint element comes from the field equivalence condition following Eqs. (19, 20). As $\mathcal{X}_m^k$ is considered as unknown when considering this kind of kinematic constraint, one has

$$\frac{1}{V_0} \int_{V_0} C_m^k \mathcal{U}_m^k\, dV = C_M^k \mathcal{U}_M^k\,, \tag{61}$$

where

$$\frac{1}{V_0} \int_{V_0} C_m^k\, dV = C_M^k\,. \tag{62}$$

From the finite element discretization of the RVE following $V_0 = \bigcup_e V_0^e$, the elementary unknowns vector is given by

$$\boldsymbol{\mathcal{U}}_e = \begin{bmatrix} \mathcal{U}_m^k \end{bmatrix}_{V_0}\,, \tag{63}$$

where $\left[\mathcal{U}_m^k\right]_{V_0}$ consists of all $\mathcal{U}_m^k$ over the volume V_0. Equation (61) is thus rewritten as

$$\frac{1}{V_0}\int_{V_0} C_m^k \mathcal{U}_m^k \, dV = \frac{1}{V_0}\sum_{V_0^e \in V_0}\int_{V_0^e} C_m^k \mathbf{N}^e \, dV \left[\mathcal{U}_m^k\right]_{V_0^e} = \mathbf{C}_e \boldsymbol{\mathcal{U}}_e \, , \qquad (64)$$

where $\mathbf{N}^e$ is the matrix of shape functions over the element V_0^e. Using Eqs. (63, 64), the elementary constraint matrix is estimated by

$$\mathbf{C}_e = \bigwedge_{V_0^e \in V_0}\left(\frac{1}{V_0}\int_{V_0^e} C_m^k \mathbf{N}^e \, dV\right) , \qquad (65)$$

where $\bigwedge_{V_0^e \in V_0}$ is the assembly operator over V_0. The kinematic matrix is given by a simple formulation

$$\mathbf{S}_e = \begin{bmatrix} C_M^k & 0 & \dots & 0 \end{bmatrix} , \qquad (66)$$

where all components of $\mathbf{S}_e$ are equal to 0 except for the first component and the dimension of $\mathbf{S}_e$ is equal to the one of the kinematic variable $\mathcal{K}_M^k$.

3.1.7 Remarks

It can be seen that Eqs. (22, 23) can be satisfied by constraining independently each component of the generalized fluctuation field following the ZFBC, MKBC, PBC, or IPBC following each pair of facets (S^i, S^{i+3}). Therefore, two categories of microscopic boundary conditions can be distinguished:

- A uniform microscopic boundary condition is obtained if one type of the kinematic constraint (ZFBC, MKBC, PBC, or IPBC) is applied to all fields (denoted by the same name ZFBC, MKBC, PBC, or IPBC respectively).
- A mixed microscopic boundary condition is obtained if the generalized fluctuation field is constrained by combining the ZFBC, MKBC, PBC, and IPBC. In this boundary condition type, the orthogonal uniform mixed boundary conditions (OUMBC) [53,54,47] can be given by combining the ZFBC and the MKBC on each facet S_i, in which the ZFBC is considered following the direction normal to the facet while the remaining directions are constrained by the MKBC.
- The kinematic constraint (23) is not always satisfied and need to be directly enforced.

In general, different kinematic constraint types lead to different macroscopic constitutive responses. The increase of the number of kinematically constrained degrees leads to a stiffer response of the homogenized behavior [27,12].

3.2 Final constraints and kinematic matrices

From the explicit representation of the constraint elements in the previous section, an arbitrary microscopic boundary (both uniform and mixed ones) described in Section 2 can be discretized into a group of possibly different constraint element

types. All constraint elements resulting from the microscopic boundary condition can be assembled to the final form

$$\mathbf{C}_b \boldsymbol{\mathcal{U}}_b - \mathbf{S}\boldsymbol{\mathcal{K}}_M = 0 \,, \tag{67}$$

where $\mathbf{C}_b$ is the final constraint matrix, $\mathbf{S}$ is the final kinematic matrix, where $\boldsymbol{\mathcal{U}}_b$ is a vector containing the unknowns of the microscopic BVP related to the constraint elements (so-called constrained unknowns)[3], and $\boldsymbol{\mathcal{K}}_M$ is the macroscopic kinematic variable vector defined by collecting all macroscopic kinematic variable vectors from the field components as

$$\boldsymbol{\mathcal{K}}_M = \left[\left(\boldsymbol{\mathcal{K}}_M^1\right)^T \ \left(\boldsymbol{\mathcal{K}}_M^2\right)^T \ \dots \ \left(\boldsymbol{\mathcal{K}}_M^{d+N}\right)^T \right]^T . \tag{68}$$

One can define the matrices $\mathbb{L}_e$, $\mathbb{T}_e$, so that for each constraint element e and for each field $\mathcal{X}_m^k$, one has

$$\boldsymbol{\mathcal{U}}_e = \mathbb{L}_e \boldsymbol{\mathcal{U}}_b \,, \text{and} \tag{69}$$
$$\boldsymbol{\mathcal{K}}_M^k = \mathbb{T}_e \boldsymbol{\mathcal{K}}_M \,. \tag{70}$$

The explicit expressions of $\mathbf{C}_b$ and $\mathbf{S}$ are easily deduced as

$$\mathbf{C}_b = \begin{bmatrix} \mathbf{C}_1 \mathbb{L}_1 \\ \mathbf{C}_2 \mathbb{L}_2 \\ \vdots \\ \mathbf{C}_{N_c} \mathbb{L}_{N_c} \end{bmatrix} \text{ and } \mathbf{S} = \begin{bmatrix} \mathbf{S}_1 \mathbb{T}_1 \\ \mathbf{S}_2 \mathbb{T}_2 \\ \vdots \\ \mathbf{S}_{N_c} \mathbb{T}_{N_c} \end{bmatrix} . \tag{71}$$

In these last equations, N_c is the number of the constraint elements resulting from the microscopic boundary condition. Clearly, with the determination of the microscopic boundary condition, all duplicate linear constraints appearing in Eq. (67) can be eliminated so that the matrix $\mathbf{C}_b$ satisfies

$$\text{rank}\,(\mathbf{C}_b) = r_{\mathbf{C}_b} \,, \tag{72}$$

where $r_{\mathbf{C}_b}$ is its number of rows.

3.3 Resolution using the multiplier elimination method

As $\boldsymbol{\mathcal{U}}_b$ is a part of the total unknowns vector $\boldsymbol{\mathcal{U}}$ of the microscopic BVP, one can decompose

$$\boldsymbol{\mathcal{U}} = \left[\boldsymbol{\mathcal{U}}_i^T \ \boldsymbol{\mathcal{U}}_b^T \right]^T \,, \tag{73}$$

where $\boldsymbol{\mathcal{U}}_i$ is the unconstrained unknowns. Eq. (67) can be rewritten as

$$\mathbf{C}\boldsymbol{\mathcal{U}} - \mathbf{S}\boldsymbol{\mathcal{K}}_M = 0 \,, \tag{74}$$

where $\mathbf{C} = \begin{bmatrix} \mathbf{0} & \mathbf{C}_b \end{bmatrix}$.

---

[3] In general, both boundary and internal degrees of freedom can be part of $\boldsymbol{\mathcal{U}}_b$ for the constraints of the type described in Section 3.1.6

3.3.1 Iterative resolution

The weak form (29) combined with the linear constraints system given in Eq. (74) results in the non-linear system of equations [59, 13]

$$
\begin{cases}
\mathbf{f}_m\left(\boldsymbol{\mathcal{U}}\right) - \mathbf{C}^T \boldsymbol{\lambda} = \mathbf{0} \\
\mathbf{C}\boldsymbol{\mathcal{U}} - \mathbf{S}\boldsymbol{\mathcal{K}}_M = \mathbf{0}
\end{cases}, \tag{75}
$$

where $\mathbf{f}_m$ is the internal force vector and where $\boldsymbol{\lambda}$ is the Lagrange multiplier vector used to enforce the constraints system (74).

In the nonlinear range, the system of equations (75) is iteratively resolved by the multiplier elimination method [57, 61], see also [59, 13]. For that purpose, the multiplier Lagrange vector $\boldsymbol{\lambda}$ is eliminated from the first equation of the system (75) using

$$
\boldsymbol{\lambda} = \mathbf{R}^T \mathbf{f}_m \,, \tag{76}
$$

where $\mathbf{R}^T = \left(\mathbf{C}\mathbf{C}^T\right)^{-1} \mathbf{C}$. The matrix inversion $\left(\mathbf{C}\mathbf{C}^T\right)^{-1}$ exists because the constraints system (74) is linearly independent as shown in Eq. (72). The system (75) is thus rewritten as

$$
\begin{cases}
\mathbf{r} = \mathbf{f}_m - \mathbf{C}^T \boldsymbol{\lambda} = \mathbf{Q}^T \mathbf{f}_m = \mathbf{0} \\
\mathbf{r}_c = \mathbf{C}\boldsymbol{\mathcal{U}} - \mathbf{S}\boldsymbol{\mathcal{K}}_M = \mathbf{0}
\end{cases}, \tag{77}
$$

where $\mathbf{r}$ is the internal force residual with $\mathbf{Q} = \mathbf{I} - \mathbf{R}\mathbf{C}$ and $\mathbf{r}_c$ is the constraint residual. The linearization of the system (77) in terms of both the increment of the unknowns vector $\Delta\boldsymbol{\mathcal{U}}$ and the increment of the macroscopic kinematic variables vector $\delta\boldsymbol{\mathcal{K}}_M$ reads [13]

$$
\begin{cases}
\mathbf{Q}^T \mathbf{K} \mathbf{Q} \Delta\boldsymbol{\mathcal{U}} + \mathbf{r} - \mathbf{V}\left(\mathbf{r}_c - \mathbf{S}\delta\boldsymbol{\mathcal{K}}_M\right) = \mathbf{0} \\
\mathbf{C}\Delta\boldsymbol{\mathcal{U}} + \mathbf{r}_c - \mathbf{S}\delta\boldsymbol{\mathcal{K}}_M = \mathbf{0}
\end{cases}, \tag{78}
$$

where $\mathbf{V} = \mathbf{Q}^T \mathbf{K} \mathbf{R}$.

The equilibrium state is obtained by considering $\delta\boldsymbol{\mathcal{K}}_M = \mathbf{0}$ in the system (78), in which case a unique solution is obtained [57]

$$
\Delta\boldsymbol{\mathcal{U}} = -\tilde{\mathbf{K}}^{-1} \tilde{\mathbf{r}} \,, \tag{79}
$$

in which

$$
\tilde{\mathbf{K}} = \mathbf{C}^T \mathbf{C} + \mathbf{Q}^T \mathbf{K} \mathbf{Q} \,, \text{ and} \tag{80}
$$

$$
\tilde{\mathbf{r}} = \mathbf{r} + \left(\mathbf{C}^T - \mathbf{V}\right) \mathbf{r}_c \,. \tag{81}
$$

The solution of $\boldsymbol{\mathcal{U}}$ at the equilibrium state is obtained by Newton-Raphson iterations.

3.3.2 Extraction of the macroscopic properties

From the finite element discretization $V_0 = \bigcup_e V_0^e$, the homogenized quantities $\boldsymbol{\mathcal{P}}_M$, $\boldsymbol{\mathcal{Z}}_M$ are estimated following the volumetric integrals (24, 27)

$$\begin{bmatrix} \boldsymbol{\mathcal{P}}_M \\ \boldsymbol{\mathcal{Z}}_M \end{bmatrix} = \frac{1}{V_0} \sum_e \int_{V_0^e} \begin{bmatrix} \boldsymbol{\mathcal{P}}_m \\ \boldsymbol{\mathcal{Z}}_m \end{bmatrix} dV . \tag{82}$$

Based on the finite element interpolation in Eq. (36), the macroscopic generalized tangent operators following Eqs. (26, 28) are estimated using Eq. (82) by

$$\begin{bmatrix} \boldsymbol{\mathcal{L}}_M & \boldsymbol{\mathcal{J}}_M \\ \boldsymbol{\mathcal{Y}}_{\boldsymbol{\mathcal{F}}_M} & \boldsymbol{\mathcal{Y}}_{\boldsymbol{\mathcal{X}}_M^C} \end{bmatrix} = \begin{bmatrix} \frac{\partial \boldsymbol{\mathcal{P}}_M}{\partial \boldsymbol{\mathcal{K}}_M} \\ \frac{\partial \boldsymbol{\mathcal{Z}}_M}{\partial \boldsymbol{\mathcal{K}}_M} \end{bmatrix} = \mathbf{D} \frac{\partial \boldsymbol{\mathcal{U}}}{\partial \boldsymbol{\mathcal{K}}_M} , \tag{83}$$

where

$$\mathbf{D} = \bigwedge_{V_0^e \in V_0} \left(\frac{1}{V_0} \int_{V_0^e} \begin{bmatrix} \boldsymbol{\mathcal{L}}_m \mathbf{B}^e & \boldsymbol{\mathcal{J}}_m \mathbf{N}^e \\ \boldsymbol{\mathcal{Y}}_{\boldsymbol{\mathcal{F}}_m} \mathbf{B}^e & \boldsymbol{\mathcal{Y}}_{\boldsymbol{\mathcal{X}}_m^C} \mathbf{N}^e \end{bmatrix} dV \right) . \tag{84}$$

In the last equation, $\mathbf{B}^e$ is the matrix of the gradients of shape functions estimated from the finite element interpolation (36); the local microscopic generalized tangent operators ($\boldsymbol{\mathcal{L}}_m$, $\boldsymbol{\mathcal{J}}_m$, $\boldsymbol{\mathcal{Y}}_{\boldsymbol{\mathcal{F}}_m}$, and $\boldsymbol{\mathcal{Y}}_{\boldsymbol{\mathcal{X}}_m^C}$) are explicitly provided through the microscopic constitutive law (12).

In order to estimate the homogenized generalized tangent operators following Eq. (83), $\frac{\partial \boldsymbol{\mathcal{U}}}{\partial \boldsymbol{\mathcal{K}}_M}$, specifying the variation of the microscopic unknowns vector $\boldsymbol{\mathcal{U}}$ with respect to the applied macroscopic kinematic variables $\boldsymbol{\mathcal{K}}_M$, should be specified. For that purpose, the system (78) is reconsidered at the equilibrium point, leading to $\mathbf{r} = \mathbf{0}$ and $\mathbf{r}_c = \mathbf{0}$, and yielding

$$\begin{cases} \mathbf{Q}^T \mathbf{K} \mathbf{Q} \delta \boldsymbol{\mathcal{U}} + \mathbf{V} \mathbf{S} \delta \boldsymbol{\mathcal{K}}_M = \mathbf{0} \\ \mathbf{C} \delta \boldsymbol{\mathcal{U}} - \mathbf{S} \delta \boldsymbol{\mathcal{K}}_M = \mathbf{0} \end{cases} . \tag{85}$$

Similarity to Eq. (78), the system (85) leads to a unique solution

$$\frac{\partial \boldsymbol{\mathcal{U}}}{\partial \boldsymbol{\mathcal{K}}_M} = \left(\tilde{\mathbf{K}} \right)^{-1} \mathbf{Y} , \tag{86}$$

where $\mathbf{Y} = \left(\mathbf{C}^T - \mathbf{V} \right) \mathbf{S}$ is the kinematic right hand sides vector and where $\tilde{\mathbf{K}}$ was already computed and possibly factorized in Eq. (80) at the converge solution.

3.4 Resolution using the constraints elimination method

By formulating under the form (67) the microscopic boundary condition presented in Section 3.1, the resolution of the microscopic BVP can be achieved by the constraints elimination method. The total unknowns vector $\boldsymbol{\mathcal{U}}$ of the microscopic BVP can be decomposed by

$$\boldsymbol{\mathcal{U}} = \begin{bmatrix} \boldsymbol{\mathcal{U}}_i \\ \boldsymbol{\mathcal{U}}_b \end{bmatrix} , \tag{87}$$

where $\mathcal{U}_i$ is the unconstrained unknowns. As all linear constraints expressed in (67) are independent, the constrained unknowns $\mathcal{U}_b$ can be divided into three parts: (i) dependent unknowns (denoted by $\mathcal{U}_d$); (ii) independent unknowns (denoted by $\mathcal{U}_f$); and (iii) direct unknowns (denoted by $\mathcal{U}_c$). The direct unknowns $\mathcal{U}_c$, whose values are directly enforced, are used to account for the zero fluctuation constraint elements described in Section 3.1.1. From each linear constraint given in each line of Eq. (67), one unique degree of freedom can be chosen and to be part of $\mathcal{U}_d$. After defining $\mathcal{U}_c$ and $\mathcal{U}_d$, $\mathcal{U}_f$ is the remaining part. From this decomposition, the constraints system (67) can be rewritten as

$$
\begin{cases}
\mathbf{C}_d \mathcal{U}_d + \mathbf{C}_f \mathcal{U}_f + \mathbf{C}_c \mathcal{U}_c = \mathbf{S}_d \mathcal{K}_M \\
\mathcal{U}_c = \mathbf{S}_c \mathcal{K}_M
\end{cases}
. \tag{88}
$$

From the choice of $\mathcal{U}_d$, the matrix $\mathbf{C}_d$ is invertible. As a result, Eq. (88) can be rewritten as

$$
\begin{cases}
\mathcal{U}_d = \mathbf{C}_{df} \mathcal{U}_f + \mathbf{S}_{df} \mathcal{K}_M \\
\mathcal{U}_c = \mathbf{S}_c \mathcal{K}_M
\end{cases}
, \tag{89}
$$

where $\mathbf{C}_{df} = -\mathbf{C}_d^{-1}\mathbf{C}_f$ and $\mathbf{S}_{df} = \mathbf{C}_d^{-1}(\mathbf{S}_d - \mathbf{C}_c\mathbf{S}_c)$. When considering the constraints system (89), the true independent unknowns of the microscopic problem are given by $\tilde{\mathcal{U}} = \begin{bmatrix} \mathcal{U}_i^T & \mathcal{U}_f^T \end{bmatrix}^T$ and Eq. (89) is rewritten as

$$
\mathcal{U} = \begin{bmatrix} \mathcal{U}_i \\ \mathcal{U}_d \\ \mathcal{U}_f \\ \mathcal{U}_c \end{bmatrix} = \mathbf{T}\tilde{\mathcal{U}} + \tilde{\mathbf{S}}\mathcal{K}_M \,, \tag{90}
$$

where

$$
\mathbf{T} = \begin{bmatrix}
\mathbf{I}_{n_i} & \mathbf{0}_{n_i \times n_f} \\
\mathbf{0}_{n_d \times n_i} & \mathbf{C}_{df} \\
\mathbf{0}_{n_f \times n_i} & \mathbf{I}_{n_f} \\
\mathbf{0}_{n_c \times n_i} & \mathbf{0}_{n_c \times n_f}
\end{bmatrix} \text{ and } \tilde{\mathbf{S}} = \begin{bmatrix}
\mathbf{0}_{n_i \times (3+N)} \\
\mathbf{S}_{df} \\
\mathbf{0}_{n_f \times (3+N)} \\
\mathbf{S}_c
\end{bmatrix} \,, \tag{91}
$$

are the constraints elimination, and the constraints kinematic matrices, respectively. In Eq. (91), n_i, n_d, n_f, and n_c are the respective dimensions of $\mathcal{U}_i$, $\mathcal{U}_d$, $\mathcal{U}_f$, and $\mathcal{U}_c$; $\mathbf{I}_n$ denotes an identity matrix of size n; and $\mathbf{0}_{n_1 \times n_2}$ denotes a zero matrix of dimensions $n_1 \times n_2$.

3.4.1 Iterative resolution

For a given value of the macroscopic kinematic variables, in the nonlinear range, the microscopic BVP is iteratively solved to find the equilibrium solution. Considering the finite element discretization of the microscopic BVP, the weak form (29) becomes

$$
\delta\mathcal{U}^T \mathbf{f}_m = 0 \,. \tag{92}
$$

The combination of Eq. (90) and Eq. (92) yields

$$
\delta\tilde{\mathcal{U}}^T \mathbf{T}^T \mathbf{f}_m = \mathbf{0} \,, \tag{93}
$$

leading to a nonlinear system of equations

$$\mathbf{T}^T\mathbf{f}_m = \mathbf{0}\,. \tag{94}$$

In order to solve iteratively the nonlinear system (94), this equation is linearized and reads at iteration $i \geq 1$

$$\mathbf{T}^T\mathbf{f}_m^{i-1} + \mathbf{T}^T\mathbf{K}\varDelta\boldsymbol{\mathcal{U}}^i = \mathbf{T}^T\mathbf{f}_m^{i-1} + \mathbf{T}^T\mathbf{K}\mathbf{T}\varDelta\tilde{\boldsymbol{\mathcal{U}}}^i = \mathbf{0}\,. \tag{95}$$

The linearized equation (95) has a unique solution

$$\varDelta\tilde{\boldsymbol{\mathcal{U}}}^i = -\tilde{\mathbf{K}}^{-1}\tilde{\mathbf{r}}^{i-1}\,, \tag{96}$$

where

$$\tilde{\mathbf{r}}^{i-1} = \mathbf{T}^T\mathbf{f}_m^{i-1}\,, \text{ and} \tag{97}$$

$$\tilde{\mathbf{K}} = \mathbf{T}^T\mathbf{K}\mathbf{T}\,. \tag{98}$$

The solution of $\boldsymbol{\mathcal{U}}$ then is then obtained by Newton-Raphson iterations.

   With the explicit formulations provided in this section, no partitioned matrices such as $\mathbf{K}_{ii}$ and no partitioned vectors such as $\mathbf{f}_{mi}$ are needed. The constraints system resulting from the microscopic boundary condition is enforced into the microscopic BVP through the use of the constraints elimination matrix $\mathbf{T}$ given in Eq. (91).

3.4.2 Extraction of the macroscopic properties

Using a similar methodology as the one described in Section 3.3.2, the homogenized generalized stress and macroscopic generalized tangent operators can be estimated. The explicit formulation of $\frac{\partial\boldsymbol{\mathcal{U}}}{\partial\boldsymbol{\mathcal{K}}_M}$ based on the system resolution of the constraints elimination method is provided in this section.

   For a variation of the macroscopic generalized kinematic variable $\delta\boldsymbol{\mathcal{K}}_M$, the variation form of the constraints system reported in (90) can be rewritten as

$$\delta\boldsymbol{\mathcal{U}} = \mathbf{T}\delta\tilde{\boldsymbol{\mathcal{U}}} + \tilde{\mathbf{S}}\delta\boldsymbol{\mathcal{K}}_M\,. \tag{99}$$

At the equilibrium state, the nonlinear system (94) is linearized as

$$\mathbf{T}^T\mathbf{K}\delta\boldsymbol{\mathcal{U}} = \mathbf{0}\,. \tag{100}$$

Combining Eqs. (99, 100), one has

$$\tilde{\mathbf{K}}\delta\tilde{\boldsymbol{\mathcal{U}}} = -\mathbf{Z}\delta\boldsymbol{\mathcal{K}}_M\,, \tag{101}$$

where $\tilde{\mathbf{K}}$ is given in Eq. (98) and where

$$\mathbf{Z} = \mathbf{T}^T\mathbf{K}\tilde{\mathbf{S}}\,. \tag{102}$$

Combining Eqs. (99, 101) yields

$$\frac{\partial\boldsymbol{\mathcal{U}}}{\partial\boldsymbol{\mathcal{K}}_M} = \tilde{\mathbf{S}} - \mathbf{T}\tilde{\mathbf{K}}^{-1}\mathbf{Z}\,. \tag{103}$$

The homogenized tangent operator is easily estimated by Eq. (83).

3.5 Remarks

In the proposed procedures, not only macroscopic material tangent operators ($\mathcal{L}_M$ and $\mathcal{J}_M$) but also the macroscopic internal tangent operators ($\mathcal{Y}_{\mathcal{F}_M}$ and $\mathcal{Y}_{\mathcal{X}_M^C}$) can be estimated in an efficient way. The global microscopic stiffness matrix does not need to be partitioned. The computation relies on the resolution of a linear system of the stiffness matrix with multiple right hand sides following either Eq. (86) when using the multiplier elimination method or Eq. (103) when using the constraints elimination method. The number of right hand sides is equal to the number of macroscopic kinematic variables $\mathcal{K}_M$ used in the macro-micro transition. Moreover, if the left hand side matrix is already used to resolve the microscopic BVP by a direct factorization procedure (*e.g.* LU factorization), this factorized matrix is still used to estimate the macroscopic tangent operators without new factorization operations. Therefore the computational time to extract the macroscopic properties of the homogenized behavior is thus negligible compared to the computation time of the resolution of the microscopic BVP.

4 Numerical examples

In this section, some finite element examples are provided to demonstrate the ability of the proposed unified treatment of microscopic boundary conditions to conduct multi-scale methods in an efficient way. First, the efficiency in terms of the computational time of the current procedure (so-called in-system procedure) is compared to the one of the condensation procedure [8] for the first-order homogenization in mechanics. Then the proposed procedure is used to estimate the macroscopic tangent operators in the cases of the homogenization of thermal field and the second-order homogenization of the mechanical field. Finally, a concurrent two-scale simulation is performed in a fully-coupled thermo-mechanical framework.

4.1 First-order homogenization

4.1.1 Computational efficiency

In this section, only mechanical analyses formulated in the first-order homogenization setting are performed. The basic constraint elementary components following Eqs. (34, 35) are simply particularized by considering

$$\begin{cases} \mathcal{K}_M^k = \mathbf{F}_M^k \text{ with } k = 1, 2, 3 \\ \mathbf{S}_m^k = \mathbf{X}_m^T \end{cases}, \tag{104}$$

where $\mathbf{F}_M^k$ is a column vector constructed from the kth row of the macroscopic deformation gradient $\mathbf{F}_M$.

The linear equilibrium system resulting from the microscopic BVP is resolved by both the Lagrange multiplier elimination procedure described in Section 3.3 (denoted by MULT_ELIM) and the constraints elimination procedure described in Section 3.4 (denoted by DISP_ELIM). The results of the homogenized tangent

operators are compared to the ones obtained by the stiffness condensation method (denoted by CONDEN) [8].

We first consider a 3-dimensional periodic microscopic structure characterized by the repeated unit cell consisting of a spherical void of radius $0.2L_{\mathrm{ref}}$ with $L_{\mathrm{ref}} = 1$ mm embedded at the center of a cube of dimensions $L_{\mathrm{ref}} \times L_{\mathrm{ref}} \times L_{\mathrm{ref}}$. To illustrate the ability of the proposed method with various RVE sizes, different RVE dimensions ranging from $L_{\mathrm{ref}} \times L_{\mathrm{ref}} \times L_{\mathrm{ref}}$ to $4L_{\mathrm{ref}} \times 4L_{\mathrm{ref}} \times L_{\mathrm{ref}}$ are used. The finite element models include 1176, 4704, 10584, and 18816 linear (8-node) brick elements, respectively. In these simulations, the material behavior is a linearly isotropic elastic model with the bulk modulus $K_m = 58.3$ GPa and the shear modulus $G_m = 26.9$ GPa.
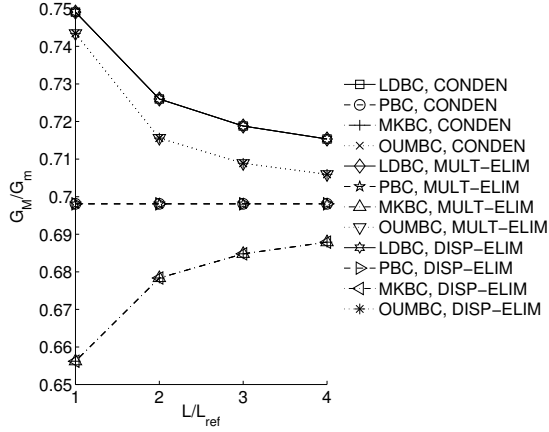
Fig. 2 Comparison of macroscopic tangent computations based on the condensation (CONDEN), current procedures including MULT_ELIM and DISP_ELIM with the convergence of the macroscopic shear modulus G_M with increasing RVE sizes for various microscopic boundary condition types (LDBC, OUMBC, PBC, MKBC).

Figure 2 shows the convergence of the homogenized shear modulus G_M with respect to the RVE size using the stiffness condensation procedure and the current approaches for different kinds of microscopic boundary conditions. The homogenized results are identical for the same boundary condition types.

Figure 3a reports the computation time needed to solve the microscopic linear equilibrium system following the constraints elimination method (denoted by DISP_ELIM) and the multiplier elimination method (denoted by MULT_ELIM) when using the PBC. Both linear (8-node) and quadratic (27-node) elements are considered. For each RVE size, the constraints elimination method allows reducing the total number of unknowns of the problems and requires less computational time in comparison with the multiplier elimination method, in which the total unknowns consist of the unknowns from all mesh nodes. When using quadratic elements, the computation time increases with the RVE size with a similar trend as using linear elements.

Figure 3b shows the computational time required to evaluate the macroscopic tangent operators using the stiffness condensation method described in[8], and the
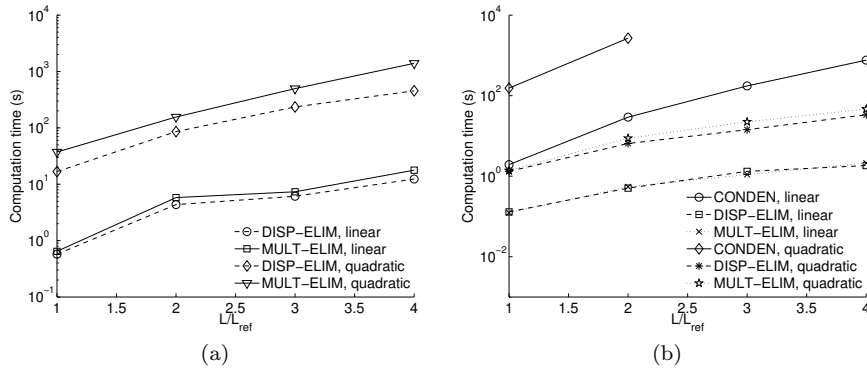
Fig. 3 Comparison of the computational time for: (a) system resolution based on the constraints elimination method (DISP_ELIM) and on the multiplier elimination method (MULT_ELIM), and (b) macroscopic tangent operators computation procedures based on the stiffness condensation (CONDEN) and current procedures (DISP_ELIM) and MULT_ELIM) in case of using the periodic boundary condition. Linear elements and quadratic elements are used in the simulations.

procedures developed herein. While the condensation method needs a significant computational time, the current procedures (DISP_ELIM and MULT_ELIM) requires a computational time much smaller. When considering a larger problem with quadratic elements, the condensation procedure could not be performed with our machine by lacks of memory (more than 30 GB reported when considering the RVE of dimensions $3L_{\text{ref}} \times 3L_{\text{ref}} \times L_{\text{ref}}$) while the developed methods could still be performed.

4.1.2 Thermal homogenization

In a thermal problem, both the macroscopic temperature T_M and its gradient $\mathbf{H}_M$ are used for the macro-micro transition. The basic constraint elementary components following Eqs. (34, 35) are particularized as

$$
\begin{cases}
\boldsymbol{\mathcal{K}}_M = \boldsymbol{\mathcal{K}}_M^1 = \left[T_M \ \mathbf{H}_M^T \right]^T \\
\mathbf{S}_m^k = \left[1 \ X_{m1} \ X_{m2} \ X_{m3} \right]
\end{cases} ,
\tag{105}
$$

where T_M is the macroscopic temperature and where $\mathbf{H}_M^T$ is the macroscopic temperature gradient. The constraints elimination method is used in this section.

The homogenized thermal conductivity of a poly-silicon layer of dimensions of $1.5\,\mu\mathrm{m} \times 1.5\,\mu\mathrm{m} \times 0.2\,\mu\mathrm{m}$ is studied. The poly-silicon layer consists of 10 grains, see Figs. 4a,b for its geometry and its finite element mesh. Each grain is identified by a number 1 to 10. Based on theoretical models and experimental measurements, the thermal conductivity of a single grain relates to its size, the impurity concentration and type [65]. As each grain has a different size, the thermal conductivity for each grain needs to be estimated and is given in Tab. 1, see [48].

As the grain intersected at the RVE boundary does not match on opposite faces, a periodic mesh can not be obtained in general. Therefore, the interpolation-based periodic boundary condition is considered with the Coons patch formulation
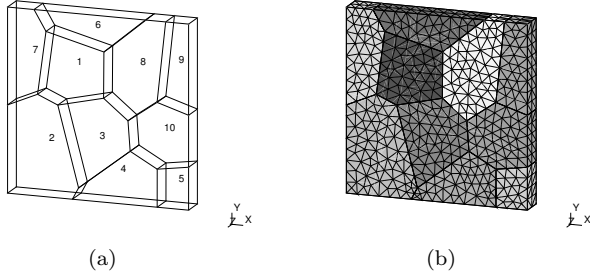
(a)   (b)

Fig. 4 A RVE geometry of a poly-silicon: (a) geometry and (b) finite element mesh

Table 1 Thermal conductivity in each grain

Grain ID	Thermal conductivity (Wm^{-1}K^{-1})	Grain ID	Thermal conductivity (Wm^{-1}K^{-1})
1	82.39	6	68.92
2	99.92	7	75.23
3	86.27	8	89.26
4	74.17	9	67.19
5	50.58	10	77.17
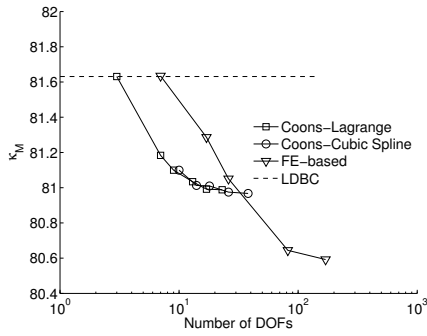
Fig. 5 Macroscopic thermal conductivity in the horizontal direction κ_M in terms of the total number of DOFs used in the interpolation basis. The one obtained by the LDBC is also reported.

based on Lagrange or cubic spline interpolants [50] and with the finite element-based formulation [63]. The obtained results are shown in Fig. 5 and compared to the one obtained by LDBC. The convergence in terms of the total number of DOFs used in the interpolation basis is observed. The interpolation-based periodic boundary condition provides a better estimation than LDBC. The converged value obtained by the IPBC based on the element-based formulation is smaller than the one obtained by the IPBC based on the patch Coons formulation as a stronger kinematic space is used in the latter. However, the method based on the Coons patch formulation is more efficient in terms of the number of DOFs required for the interpolation basis.

4.2 Second-order mechanical homogenization

In the second-order mechanical FE^2 scheme [10], the macro-scale gradient of the deformation gradient, denoted by $\mathbf{G}_M = \mathbf{F}_M \otimes \boldsymbol{\nabla}_0$, is used as a kinematic variable besides $\mathbf{F}_M$. Therefore both $\mathbf{F}_M$ and $\mathbf{G}_M$ must be considered in the macro-micro scale transition when defining the second-order microscopic boundary condition. The basic constraint elementary components following Eqs. (34, 35) are particularized by considering

$$\begin{cases} \boldsymbol{\mathcal{K}}_M^k = & [F_{Mk1}\ F_{Mk2}\ F_{Mk3}\ G_{Mk11}\ G_{Mk12}\ G_{Mk13} \\ & G_{Mk21}\ G_{Mk22}\ G_{Mk23}\ G_{Mk31}\ G_{Mk32}\ G_{Mk33}]^T \\ \mathbf{S}_m^k = & [X_{m1}\ X_{m2}\ X_{m3}\ X_{sq11}\ X_{sq12}\ X_{sq13} \\ & X_{sq21}\ X_{sq22}\ X_{sq23}\ X_{sq31}\ X_{sq32}\ X_{sq33}] \\ & \text{with } k = 1, 2, 3 \end{cases}, \qquad (106)$$

where $\mathbf{X}_{sq} = \frac{1}{2}\mathbf{X}_m \otimes \mathbf{X}_m$. The unit cell of dimensions $L_{\text{ref}} \times L_{\text{ref}} \times L_{\text{ref}}$ consisting of 1176 quadratic brick elements as described in Section 4.1.1 is used. The macroscopic tangent operators are estimated by the multiplier elimination approach (MULT_ELIM). As the mesh is periodic, LDBC, IPBC, and PBC are used for the comparison purpose.

The results of the macroscopic in-plane shear modulus G_M and of the second-order modulus J_M (component 112112) obtained by the LDBC, IPBC, and PBC in terms of the total number of DOFs used in the IPBC basis are shown in Figs. 6a and b, respectively. The macroscopic tangent properties given by the IPBC are bounded by the ones given by the LDBC and the PBC and converge when increasing the total number of DOFs used in the interpolation basis. The IPBC results based on the finite elements converge to the ones given by the PBC, while the IPBC results based on the patch Coons formulations are stiffer as a results of a stronger kinematic statement. However, the interpolation method based on the Coons patch formulation (both Lagrange and cubic spline) is more efficient in terms of the number of DOFs used in the interpolation basis.
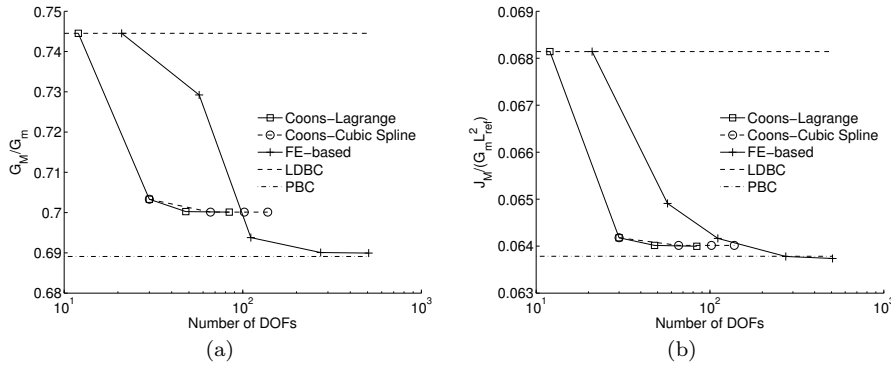

Fig. 6 Second-order interpolation-based periodic boundary condition : (a) macroscopic in-plane shear modulus G_M and (b) macroscopic second-order modulus J_M in terms of the total number of degrees of freedom (DOFs) used in the interpolation basis of the IPBC. The ones obtained by the LDBC and the PBC are also reported.

4.3 Fully-coupled thermo-mechanical two-scale problem
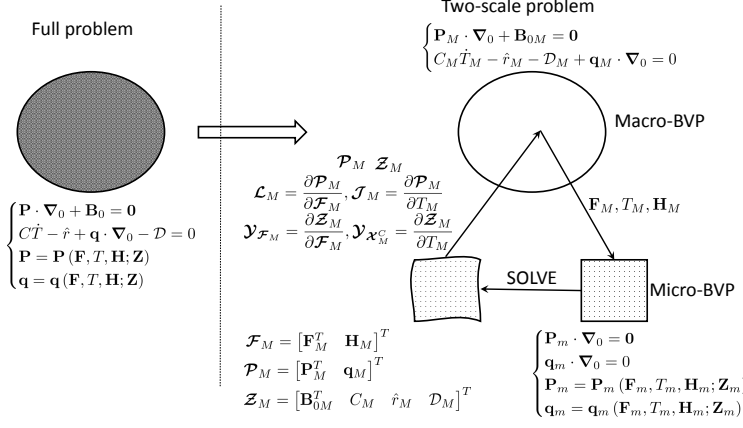
4.3.1 Multi-scale strategy

Fig. 7 Two-scale strategy for fully-coupled thermo-mechanical problems

For a problem with evolving microstructure, the direct solution could not be performed as an enormous numerical system arises. A two-scale modeling strategy is defined by introducing two BVPs, one at the micro-scale (denoted with the subscript m) and one at the macro-scale (denoted with the subscript M), see Fig. 7. The macroscopic BVP takes the form [66,67]

$$\begin{cases} \mathbf{P}_M \cdot \boldsymbol{\nabla}_0 + \mathbf{B}_{0M} = \mathbf{0} \\ C_M \dot{T}_M - \hat{r}_M - \mathcal{D}_M + \mathbf{q}_M \cdot \boldsymbol{\nabla}_0 = 0 \end{cases}, \tag{107}$$

where $\mathbf{P}_M$ is the first Piola-Kirchhoff stress tensor, $\mathbf{B}_{0M}$ is the body force, C_M is the macroscopic heat capacity per unit temperature, $\hat{r}_M$ is the macroscopic external heat supply, $\mathbf{q}_M$ is the macroscopic heat flux vector per unit reference surface, and $\mathcal{D}_M$ is the macroscopic mechanical dissipation. The required constitutive relations

$$\begin{cases} \mathbf{P}_M = \mathbf{P}_M \left(\mathbf{F}_M, T_M, \mathbf{H}_M; \mathbf{Z}_M \right) \\ \mathbf{q}_M = \mathbf{q}_M \left(\mathbf{F}_M, T_M, \mathbf{H}_M; \mathbf{Z}_M \right) \end{cases}, \tag{108}$$

as well as $\mathbf{B}_{0M}$, c_M, $\hat{r}_M$ and $\mathcal{D}_M$ are obtained from the microscopic BVP. By assuming the microscopic characteristic time and length are much smaller than their macroscopic counterparts [17,19], the microscopic BVP is simplified under the steady state assumption by

$$\begin{cases} \mathbf{P}_m \cdot \boldsymbol{\nabla}_0 = 0 \\ \mathbf{q}_m \cdot \boldsymbol{\nabla}_0 = 0 \end{cases}, \tag{109}$$

with the constitutive relations

$$
\begin{cases}
\mathbf{P}_m = \mathbf{P}_m \left(\mathbf{F}_m, T_m, \mathbf{H}_m; \mathbf{Z}_m \right) \\
\mathbf{q}_m = \mathbf{q}_m \left(\mathbf{F}_m, T_m, \mathbf{H}_m; \mathbf{Z}_m \right)
\end{cases}
, \tag{110}
$$

explicitly known as the constitutive behavior of the material laws associated to the microstructure constituents. Possible microscopic boundary condition types and the finite element resolution of the microscopic problem were discussed in the previous sections. The basic constraint elementary components following Eqs. (34, 35) are particularized as

$$
\begin{cases}
\boldsymbol{\mathcal{K}}_M^k = \begin{cases}
\begin{bmatrix} F_{Mk1} \ F_{Mk2} \ F_{Mk3} \end{bmatrix}^T & \text{with } k = 1, 2, 3 \\
\begin{bmatrix} T_M \ H_{M1} \ H_{M2} \ H_{M3} \end{bmatrix}^T & \text{with } k = 4
\end{cases} \\
\mathbf{S}_m^k = \begin{cases}
\begin{bmatrix} X_{m1} \ X_{m2} \ X_{m3} \end{bmatrix} & \text{with } k = 1, 2, 3 \\
\begin{bmatrix} 1 \ X_{m1} \ X_{m2} \ X_{m3} \end{bmatrix} & \text{with } k = 4
\end{cases}
\end{cases}
. \tag{111}
$$

Besides the first Piola-Kirchhoff stress and the heat flux vector, the body force $\mathbf{B}_{0M}$, the macroscopic heat capacity per unit temperature C_M, the macroscopic external heat supply $\hat{r}_M$, and the macroscopic mechanical dissipation $\mathcal{D}_M$ are upscaled by defining $\boldsymbol{\mathcal{Z}}$ in Eq. (27) as

$$
\boldsymbol{\mathcal{Z}}_m = \begin{bmatrix} \mathbf{B}_{0m}^T \ C_m \ \hat{r}_m \ \mathcal{D}_m \end{bmatrix}^T \text{ and } \boldsymbol{\mathcal{Z}}_M = \begin{bmatrix} \mathbf{B}_{0M}^T \ C_M \ \hat{r}_M \ \mathcal{D}_M \end{bmatrix}^T. \tag{112}
$$

4.3.2 Numerical application

In this section, the thermo-mechanically loaded plate is considered, see Fig. 8. The infinitely long plate is made from a particle reinforced composite material with spherical inclusions which are periodically distributed in a matrix and with a fiber fraction of 30 %, see Fig. 8a. The inclusion diameter of 137 μm is much smaller than the macroscopic dimensions of the plate (30 mm $\times$ 1200 mm), which allows formulating a macro-scale plane strain problem while considering a three-dimensional representative volume element at the micro-scale, see Fig. 8b. The geometry and boundary conditions at the macro-scale are the same as considered in [17].
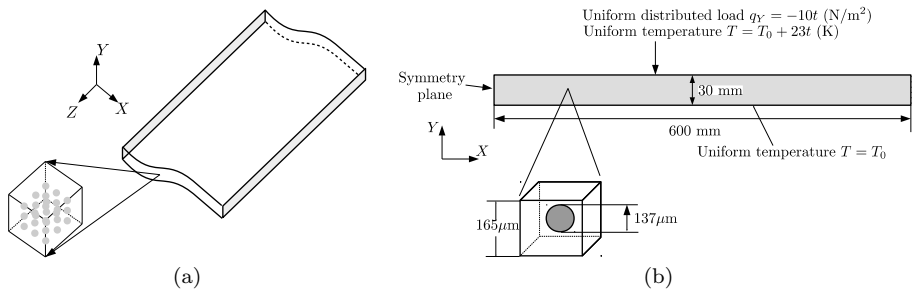

Fig. 8 A two-scale thermo-mechanical test: (a) geometry and (b) two-scale model with macroscopic boundary conditions and representative volume element

Table 2 Material constants at the reference temperature $T_0 = 293$ K [17]

Constant	Notation (unit)	Matrix	Fiber
Bulk modulus	K (GPa)	73.53	213.89
Shear modulus	μ (GPa)	28.19	160.42
Initial yield stress	τ_{y0} (MPa)	300	
Hardening modulus	H_0 (MPa)	150	
Thermal expansion coefficient	α ($10^{-6}\mathrm{K}^{-1}$)	23.6	5
Thermal conductivity	κ ($\mathrm{Wm}^{-1}\mathrm{K}^{-1}$)	247	38
Specific heat capacity	C ($10^6\,\mathrm{Jm}^{-3}\mathrm{K}^{-1}$)	2.43	3.38

The reference configuration is defined at the initial temperature $T_0 = 293$ K. Due to the symmetry of the macroscopic problem, a half of plate is studied. The plate is clamped on its right side. The symmetry condition is considered for the left side. At the top side, a uniformly-distributed load is applied following the vertical direction by a time-dependent function $q_Y = -10t$ Nm^{-2}, and the temperature is prescribed by a time-dependent function $T = T_0 + 23t$ K, where T_0 is the initial temperature. The bottom side is stress-free and its temperature is kept constant to the initial value T_0. The microscopic problem is considered in a cubic representative volume element of dimensions 165 μm $\times$ 165 μm $\times$ 165 μm with a spherical inclusion of diameter 137 μm.

The matrix is modeled by a thermo-J_2-elastoplastic constitutive model, see Appendix B. The strain hardening behavior is characterized by a linear hardening law coupled with a linear thermal softening as

$$\tau_y\left(\gamma, T_m\right) = \left(\tau_{y0} + H_0\gamma\right)\left[1 - \omega_T\left(T_m - T_0\right)\right], \tag{113}$$

where τ_{y0} is the initial yield stress, where H_0 is the hardening modulus at the reference temperature T_0, where γ is the equivalent plastic strain, and where ω_T is the thermal softening modulus. In this section, a constant value of $\omega_T = 0.002$ K^{-1} is considered. The thermo-plastic heating is characterized by the Taylor-Quinney factor β whose value is 0.9 and kept constant during the simulation. The fibers obey to a linearly elastic constitutive law. The material constants of the matrix and the fibers at the initial temperature $T_0 = 293$ K are detailed in Tab. 2. The fiber-matrix interface is assumed to be perfectly bonded.

The microscopic BVP is resolved by the multiplier elimination approach described in Section 3.3. For comparison purpose, the problem is analyzed with the PBC and the IPBC. The IPBC is considered with the patch Coons formulation based on the Lagrange interpolant of order 9 and the cubic spline interpolant of order 5. The simulations are performed until the final time of 10 s.

To assess the choice of the time step size, the multi-scale simulations are first conducted using the PBC with different step sizes, leading to 10, 25 and 40 steps. The homogenized responses in terms of the horizontal reaction force versus the vertical displacement of the section at the symmetry plane are depicted in Fig. 9a, showing that the time step size corresponding to 25 steps can be used to ensure the accuracy.

The results given by the IPBC based on the Coons patch formulation are compared to the one given by the PBC in Fig. 9b. The results given by the Lagrange and cubic spline interpolants coincide as the interpolation orders used are enough to capture the deformation modes. The IPBC results in a stronger kinematic space
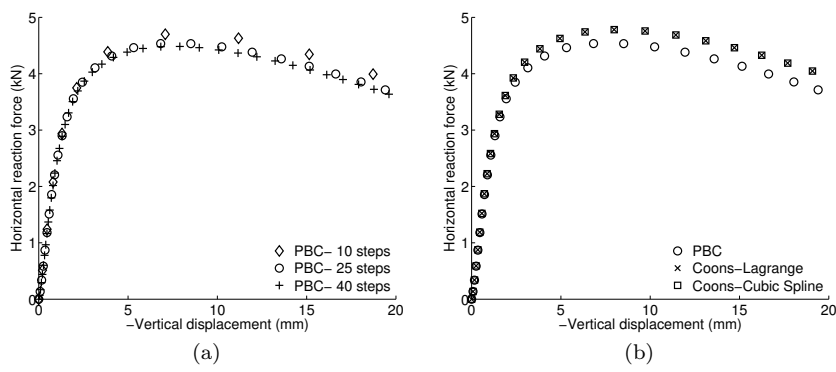
Fig. 9 Horizontal reaction force versus vertical displacement of the section at the symmetry plane: (a) influence of number of time steps when using PBC and (b) results comparison for 25 time steps

as compared to the PBC as discussed in previous sections, and leads to a stiffer homogenized behavior. The two-scale solution using the PBC is presented in Fig. 10 at the final time (t = 10 s). The equivalent plastic strain and the temperature distribution at the microscopic scale are shown.
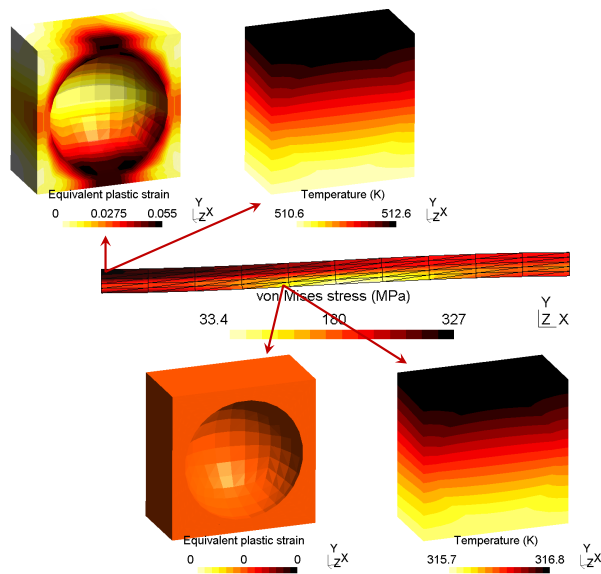

Fig. 10 Two-scale solution with the PBC at the final time t=10 s

5 Conclusion

In this work, a unified approach is developed, which allows enforcing arbitrary types of microscopic boundary conditions in multi-scale analyses. The microscopic boundary condition leads to a system of multi-point linear constraints. In order to enforce these constraints into the microscopic finite element equations, two methods based on the Lagrange multiplier elimination and on the constraints elimination are described. From the linearized system of the nonlinear equations of the microscopic BVP, the macroscopic tangent operators can be directly estimated without any significant computational cost. The capability of the proposed procedure is demonstrated in the microscopic analyses as well as in a fully-coupled thermo-mechanical two-scale problem.

A Tensor-vector conversion rule

Considering an arbitrary 3-dimensional n^{th} order tensor $\mathbf{A} = A_{i_1 i_2 \ldots i_n}$, all its components can be rewritten in a vector $\mathbf{B}$ with one index k by

$$\mathbf{B} = \text{vec}\,(\mathbf{A}) \leftrightarrow B_k = A_{i_1 i_2 \ldots i_n} \text{ with } k = i_n + 3^1(i_{n-1} - 1) + \ldots + 3^{n-1}(i_1 - 1), \quad (114)$$

where $\mathbf{B}$ is a vector of 3^n components. With an arbitrary tensor group $\boldsymbol{\mathcal{A}} = \begin{bmatrix} \mathbf{A}_1^T & \ldots & \mathbf{A}_N^T \end{bmatrix}^T$, its vector representation is defined by

$$\text{vec}\,(\boldsymbol{\mathcal{A}}) = \begin{bmatrix} \text{vec}\,(\mathbf{A}_1) \\ \vdots \\ \text{vec}\,(\mathbf{A}_N) \end{bmatrix}. \quad (115)$$

B Fully-thermomechanical J_2 elastoplastic material law

Under the large deformation framework, the deformation gradient $\mathbf{F}$, whose Jacobian $J = \det \mathbf{F} > 0$, can be decomposed as

$$\mathbf{F} = \mathbf{F}_e \cdot \mathbf{F}_p, \quad (116)$$

where $\mathbf{F}_e$ and $\mathbf{F}_p$ represent respectively the elastic and plastic parts satisfying $\det \mathbf{F}_e = J$ and $\det \mathbf{F}_p = 1$. The material model is based on the hyperelastic assumption with an elastic potential given by

$$U\,(\mathbf{C}^e, T) = \frac{K}{2} \left[\ln J - 3\alpha\,(T - T_0) \right]^2 + \frac{G}{4} \text{dev}\,(\ln \mathbf{C}_e) : \text{dev}\,(\ln \mathbf{C}_e), \quad (117)$$

where $\text{dev}\,\bullet$ and $\text{tr}\,\bullet$ represent the deviatoric and trace operators, where K and G are bulk and shear moduli, where α is the thermal dilatation coefficient, where T and T_0 are the current and initial temperatures, and where $\mathbf{C}_e = \mathbf{F}_e^T \cdot \mathbf{F}_e$ is the elastic right Cauchy strain tensor. The logarithmic mechanical elastic strain tensor is defined by

$$\mathbf{E}_e = \frac{1}{2} \ln \mathbf{C}_e. \quad (118)$$

Equation (117) can be rewritten as

$$U = \frac{K}{2} \left[\text{tr} \, \mathbf{E}_e - 3\alpha \left(T - T_0 \right) \right]^2 + G \text{dev} \, \mathbf{E}_e : \text{dev} \, \mathbf{E}_e \,. \tag{119}$$

During the elastic stage, the first Piola-Kirchhoff stress can be estimated by

$$\mathbf{P} = \frac{\partial U}{\partial \mathbf{F}} = 2\mathbf{F}_e \cdot \frac{\partial U}{\partial \mathbf{C}_e} \cdot \mathbf{F}_p^{-T} = \mathbf{F}_e \cdot (\boldsymbol{\tau} : \boldsymbol{\mathcal{L}}) \cdot \mathbf{F}_p^{-T} \,, \tag{120}$$

where

$$\boldsymbol{\mathcal{L}} = \frac{\partial \ln \mathbf{C}_e}{\partial \mathbf{C}_e} \,, \tag{121}$$

and where

$$\boldsymbol{\tau} = \frac{\partial U}{\partial \mathbf{E}_e} = \left(K \mathbf{I} \otimes \mathbf{I} + 2G \boldsymbol{\mathcal{I}}^{dev} \right) : \mathbf{E}_e - 3K\alpha \left(T - T_0 \right) \mathbf{I} \,. \tag{122}$$

It can be shown that the stress measure $\boldsymbol{\tau}$ is the Kirchhoff stress expressed in the elastic corotational space [68].

The J_2 elastoplastic model is considered with the von Mises yield surface in the corotational space

$$\tau_{eq} - \tau_y \left(\gamma, T \right) \leq 0 \,, \tag{123}$$

where $\tau_{eq} = \sqrt{\frac{3}{2} \text{dev} \, \boldsymbol{\tau} : \text{dev} \, \boldsymbol{\tau}}$, and where τ_y is the yield stress, which depends on the equivalent plastic strain γ and on the temperature. The strain hardening modulus and thermal softening modulus can be respectively defined by

$$H_\gamma = \frac{\partial \tau_y}{\partial \gamma} \geq 0 \text{ and } H_T = \frac{\partial \tau_y}{\partial T} \leq 0 \,. \tag{124}$$

The plastic deformation evolution follows an associated flow rule by

$$\mathbf{D}_p = \dot{\mathbf{F}}_p \cdot \mathbf{F}_p^{-1} = \dot{\gamma} \mathbf{N} \,, \tag{125}$$

where $\dot{\gamma}$ is the equivalent plastic strain rate and where $\mathbf{N}$ is the flow normal given by

$$\mathbf{N} = \frac{\partial f}{\partial \boldsymbol{\tau}} = \frac{3}{2} \frac{\text{dev} \, \boldsymbol{\tau}}{\tau_{eq}} \,. \tag{126}$$

The thermal flux can be expressed in the reference configuration from a mapping of the Fourier law defined in the current configuration by

$$\mathbf{q} = J \left(\kappa \boldsymbol{\nabla} T \right) \cdot \mathbf{F}^{-T} = \boldsymbol{\chi} \cdot \boldsymbol{\nabla}_0 T \,, \tag{127}$$

where κ is the thermal conductivity and where

$$\boldsymbol{\chi} = J\kappa \left(\mathbf{F}^{-1} \cdot \mathbf{F}^{-T} \right) \,. \tag{128}$$

At a temperature T, the resolution of the system of Eqs. (120, 122, 123, 125) follows the predictor-corrector scheme during the time interval $[t_n \ t_{n+1}]$ as described in [69]. The elastic and plastic powers are respectively estimated by the relations

$$\dot{W}^{el} = \mathbf{P} : \left(\dot{\mathbf{F}}_e \cdot \mathbf{F}_p \right) \,, \text{ and } \dot{W}^p = \mathbf{P} : \left(\mathbf{F}_e \cdot \dot{\mathbf{F}}_p \right) \,. \tag{129}$$

Using Eqs. (123, 125), one has

$$\dot{W}^p = \mathbf{P} : \left(\mathbf{F}_e \cdot \mathbf{D}_p \cdot \mathbf{F}_p \right) = \boldsymbol{\tau} : \mathbf{D}_p = \dot{\gamma} \boldsymbol{\tau} : \frac{3}{2} \frac{\text{dev} \, \boldsymbol{\tau}}{\tau_{eq}} = \dot{\gamma} \tau_y \,. \tag{130}$$

The mechanical source $\mathcal{D}$ is thus given by

$$\mathcal{D} = \beta \dot{\gamma} \tau_y + T \frac{\partial \dot{W}^{el}}{\partial T} \,, \tag{131}$$

where β is the TaylorQuinney factor.

References

1. J. Guedes, N. Kikuchi, Computer Methods in Applied Mechanics and Engineering **83**(2), 143 (1990). DOI 10.1016/0045-7825(90)90148-F. Cited By 679
2. R. Smit, W. Brekelmans, H. Meijer, Computer Methods in Applied Mechanics and Engineering **155**(1-2), 181 (1998). Cited By 262
3. C. Miehe, J. Schotte, J. Schrder, Computational Materials Science **16**(1-4), 372 (1999). Cited By 88
4. J. Michel, H. Moulinec, P. Suquet, Computer Methods in Applied Mechanics and Engineering **172**(1-4), 109 (1999). DOI http://dx.doi.org/10.1016/S0045-7825(98)00227-8. URL http://www.sciencedirect.com/science/article/pii/S0045782598002278
5. F. Feyel, J.L. Chaboche, Computer Methods in Applied Mechanics and Engineering **183**(3-4), 309 (2000). Cited By 346
6. M.G.D. Geers, V.G. Kouznetsova, W.A.M. Brekelmans, Journal of Computational and Applied Mathematics **234**(7), 2175 (2010). DOI DOI: 10.1016/j.cam.2009.08.077. URL http://www.sciencedirect.com/science/article/B6TYH-4X1J73B-8/2/ee8d9b69133503eaf14b00ddbe1bd8f5. Fourth International Conference on Advanced COmputational Methods in ENgineering (ACOMEN 2008)
7. V. Kouznetsova, W.A.M. Brekelmans, F.P.T. Baaijens, Computational Mechanics **27**(1), 37 (2001). URL http://dx.doi.org/10.1007/s004660000212
8. C. Miehe, A. Koch, Archive of Applied Mechanics **72**(4), 300 (2002). URL http://dx.doi.org/10.1007/s00419-002-0212-2. 10.1007/s00419-002-0212-2
9. T. Kanit, S. Forest, I. Galliet, V. Mounoury, D. Jeulin, International Journal of Solids and Structures **40**(13-14), 3647 (2003). DOI DOI: 10.1016/S0020-7683(03)00143-4. URL http://www.sciencedirect.com/science/article/B6VJS-48GDV9K-1/2/2dd6cda9c49706ed2c969bdea531bb50
10. V.G. Kouznetsova, M.G.D. Geers, W.A.M. Brekelmans, Computer Methods in Applied Mechanics and Engineering **193**(48-51), 5525 (2004). DOI DOI: 10.1016/j.cma.2003.12.073. URL http://www.sciencedirect.com/science/article/B6V29-4D4D4JV-3/2/6fd8ac06299b9a26d8a17438871de868. Advances in Computational Plasticity
11. L. Kaczmarczyk, C.J. Pearce, N. Bićanić, Int. J. Numer. Meth. Engng. **74**(3), 506 (2008). URL http://dx.doi.org/10.1002/nme.2188
12. D. Peric, E.A. de Souza Neto, R.A. Feijóo, M. Partovi, A.J.C. Molina, Int. J. Numer. Meth. Engng. (2010). URL http://dx.doi.org/10.1002/nme.3014
13. V.D. Nguyen, L. Noels, International Journal of Solids and Structures **51**(1112), 2183 (2014). DOI http://dx.doi.org/10.1016/j.ijsolstr.2014.02.029. URL http://www.sciencedirect.com/science/article/pii/S0020768314000778
14. E. Bosco, V.G. Kouznetsova, M.G.D. Geers, International Journal for Numerical Methods in Engineering **102**(3-4), 496 (2015). DOI 10.1002/nme.4838. URL http://dx.doi.org/10.1002/nme.4838
15. I. Özdemir, W.A.M. Brekelmans, M.G.D. Geers, International Journal for Numerical Methods in Engineering **73**(2), 185 (2008). DOI 10.1002/nme.2068. URL http://dx.doi.org/10.1002/nme.2068
16. E. Monteiro, J. Yvonnet, Q. He, Computational Materials Science **42**(4), 704 (2008). DOI http://dx.doi.org/10.1016/j.commatsci.2007.11.001. URL http://www.sciencedirect.com/science/article/pii/S0927025607003242
17. I. Özdemir, W. Brekelmans, M. Geers, Computer Methods in Applied Mechanics and Engineering **198**(34), 602 (2008). DOI http://dx.doi.org/10.1016/j.cma.2008.09.008. URL http://www.sciencedirect.com/science/article/pii/S0045782508003277
18. I. Temizer, P. Wriggers, Journal of the Mechanics and Physics of Solids **59**(2), 344 (2011). DOI http://dx.doi.org/10.1016/j.jmps.2010.10.004. URL http://www.sciencedirect.com/science/article/pii/S002250961000219X
19. A. Sengupta, P. Papadopoulos, R.L. Taylor, International Journal for Numerical Methods in Engineering **91**(13), 1386 (2012). DOI 10.1002/nme.4320. URL http://dx.doi.org/10.1002/nme.4320
20. J. Schröder, M.A. Keip, in *Computer Methods in Mechanics*, *Advanced Structured Materials*, vol. 1, ed. by M. Kuczma, K. Wilmanski (Springer Berlin Heidelberg, 2010), pp. 311–329

21. M.A. Keip, P. Steinmann, J. SchrJöder, Computer Methods in Applied Mechanics and Engineering **278**, 62 (2014). DOI http://dx.doi.org/10.1016/j.cma.2014.04.020. URL http://www.sciencedirect.com/science/article/pii/S0045782514001455
22. J. Schröder, M.A. Keip, Computational Mechanics **50**(2), 229 (2012)
23. A. Javili, G. Chatzigeorgiou, P. Steinmann, International Journal of Solids and Structures **50**(2526), 4197 (2013). DOI http://dx.doi.org/10.1016/j.ijsolstr.2013.08.024. URL http://www.sciencedirect.com/science/article/pii/S0020768313003405
24. C. Miehe, D. Vallicotti, S. Teichtmeister, GAMM-Mitteilungen **38**(2), 313 (2015). DOI 10.1002/gamm.201510017. URL http://dx.doi.org/10.1002/gamm.201510017
25. J. Schröder, M. Labusch, M.A. Keip, Computer Methods in Applied Mechanics and Engineering pp. – (2015). DOI http://dx.doi.org/10.1016/j.cma.2015.10.005. URL http://www.sciencedirect.com/science/article/pii/S0045782515003242
26. Z.F. Khisaeva, M. Ostoja-Starzewski, Journal of Elasticity **85**(2), 153 (2006). DOI 10.1007/s10659-006-9076-y. URL http://dx.doi.org/10.1007/s10659-006-9076-y
27. M. Ostoja-Starzewski, Probabilistic Engineering Mechanics **21**(2), 112 (2006). DOI http://dx.doi.org/10.1016/j.probengmech.2005.07.007. URL http://www.sciencedirect.com/science/article/pii/S0266892005000433
28. T. Hoang, M. Guerich, J. Yvonnet, Journal of Engineering Mechanics p. Accepted (2015). URL https://hal-upec-upem.archives-ouvertes.fr/hal-01228966
29. J.G.F. Wismans, L.E. Govaert, J.A.W. van Dommelen, Journal of Polymer Science Part B: Polymer Physics **48**(13), 1526 (2010). DOI 10.1002/polb.22055. URL http://dx.doi.org/10.1002/polb.22055
30. G. Legrain, P. Cartraud, I. Perreard, N. Moes, International Journal for Numerical Methods in Engineering **86**(7), 915 (2011). DOI 10.1002/nme.3085. URL http://dx.doi.org/10.1002/nme.3085
31. H. Kumar, C. Briant, W. Curtin, Mechanics of Materials **38**(810), 818 (2006). DOI http://dx.doi.org/10.1016/j.mechmat.2005.06.030. URL http://www.sciencedirect.com/science/article/pii/S0167663605001638. Advances in Disordered Materials
32. B. Sonon, B. François, T.J. Massart, Computational Mechanics **56**(2), 221 (2015). DOI 10.1007/s00466-015-1168-8. URL http://dx.doi.org/10.1007/s00466-015-1168-8
33. V.P. Nguyen, O. Lloberas-Valls, M. Stroeven, L.J. Sluys, Computer Methods in Applied Mechanics and Engineering **199**(4548), 3028 (2010). DOI http://dx.doi.org/10.1016/j.cma.2010.06.018. URL http://www.sciencedirect.com/science/article/pii/S0045782510001854
34. V.P. Nguyen, O. Lloberas-Valls, M. Stroeven, L.J. Sluys, International Journal for Numerical Methods in Engineering **89**(2), 192 (2012). DOI 10.1002/nme.3237. URL http://dx.doi.org/10.1002/nme.3237
35. E. Coenen, V. Kouznetsova, M. Geers, International Journal for Numerical Methods in Engineering **90**(1), 1 (2012). DOI 10.1002/nme.3298. URL http://dx.doi.org/10.1002/nme.3298
36. L. Wu, D. Tjahjanto, G. Becker, A. Makradi, A. Jérusalem, L. Noels, Engineering Fracture Mechanics **104**, 162 (2013). DOI http://dx.doi.org/10.1016/j.engfracmech.2013.03.018. URL http://www.sciencedirect.com/science/article/pii/S0013794413001252
37. M. Mosby, K. Matouš, Modelling and Simulation in Materials Science and Engineering **23**(8), 085014 (2015). URL http://stacks.iop.org/0965-0393/23/i=8/a=085014
38. M. Ostoja-Starzewski, X. Wang, Computer Methods in Applied Mechanics and Engineering **168**(14), 35 (1999). DOI http://dx.doi.org/10.1016/S0045-7825(98)00105-4
39. X. Yin, W. Chen, A. To, C. McVeigh, W. Liu, Computer Methods in Applied Mechanics and Engineering **197**(43 - 44), 3516 (2008). DOI http://dx.doi.org/10.1016/j.cma.2008.01.008. Stochastic Modeling of Multiscale and Multiphysics Problems
40. A. Liebscher, C. Proppe, C. Redenbach, D. Schwarzer, Probabilistic Engineering Mechanics **28**, 143 (2012). DOI http://dx.doi.org/10.1016/j.probengmech.2011.08.015. URL http://www.sciencedirect.com/science/article/pii/S0266892011000701. Computational Stochastic Mechanics {CSM6}
41. G. Stefanou, D. Savvas, M. Papadrakakis, Composite Structures **132**, 384 (2015). DOI http://dx.doi.org/10.1016/j.compstruct.2015.05.044. URL http://www.sciencedirect.com/science/article/pii/S0263822315004183
42. P. Trovalusci, M.L. De Bellis, M. Ostoja-Starzewski, A. Murrali, Meccanica **49**(11), 2719 (2014)

43. P. Trovalusci, M. Ostoja-Starzewski, M.L. De Bellis, A. Murrali, European Journal of Mechanics-A/Solids **49**, 396 (2015)
44. J. Ma, S. Sahraee, P. Wriggers, L. De Lorenzis, Computational Mechanics pp. 1–17 (2015)
45. D. Pivovarov, P. Steinmann, Computational Mechanics **57**(1), 123 (2016)
46. X. Yin, S. Lee, W. Chen, W.K. Liu, M.F. Horstemeyer, Journal of Mechanical Design **131**(2) (2009). DOI http://dx.doi.org/10.1115/1.3042159
47. V. Lucas, J.C. Golinval, S. Paquay, V.D. Nguyen, L. Noels, L. Wu, Computer Methods in Applied Mechanics and Engineering **294**, 141 (2015). DOI http://dx.doi.org/10.1016/j.cma.2015.05.019. URL http://www.sciencedirect.com/science/article/pii/S0045782515001929
48. L. Wu, V. Lucas, V.D. Nguyen, J.C. Golinval, S. Paquay, L. Noels, Computer Methods in Applied Mechanics and Engineering **310**, 802 (2016). DOI http://dx.doi.org/10.1016/j.cma.2016.07.042. URL http://www.sciencedirect.com/science/article/pii/S0045782516303930
49. S.D. Mesarovic, J. Padbidri, Philosophical Magazine **85**(1), 65 (2005). DOI 10.1080/14786430412331313321
50. V.D. Nguyen, E. Béchet, C. Geuzaine, L. Noels, Computational Materials Science **55**(0), 390 (2012). DOI 10.1016/j.commatsci.2011.10.017. URL http://www.sciencedirect.com/science/article/pii/S0927025611005866
51. K. Matouš, M.G. Kulkarni, P.H. Geubelle, Journal of the Mechanics and Physics of Solids **56**(4), 1511 (2008). DOI http://dx.doi.org/10.1016/j.jmps.2007.08.005. URL http://www.sciencedirect.com/science/article/pii/S0022509607001718
52. C. Hirschberger, S. Ricker, P. Steinmann, N. Sukumar, Engineering Fracture Mechanics **76**(6), 793 (2009). DOI http://dx.doi.org/10.1016/j.engfracmech.2008.10.018. URL http://www.sciencedirect.com/science/article/pii/S0013794408002993. Multi-scale analysis of evolving interfaces in (multi) materialsMulti-scale Analysis
53. S. Hazanov, M. Amieur, International Journal of Engineering Science **33**(9), 1289 (1995). DOI http://dx.doi.org/10.1016/0020-7225(94)00129-8. URL http://www.sciencedirect.com/science/article/pii/0020722594001298
54. D.H. Pahr, P.K. Zysset, Biomechanics and Modeling in Mechanobiology **7**(6), 463 (2007). DOI 10.1007/s10237-007-0109-7. URL http://dx.doi.org/10.1007/s10237-007-0109-7
55. B.S. Mercer, K.K. Mandadapu, P. Papadopoulos, Computer Methods in Applied Mechanics and Engineering **286**, 268 (2015). DOI http://dx.doi.org/10.1016/j.cma.2014.12.021. URL http://www.sciencedirect.com/science/article/pii/S0045782514005003
56. H.M. Inglis, P.H. Geubelle, K. Matouš, Philosophical Magazine **88**(16), 2373 (2008). DOI 10.1080/14786430802345645
57. M. Ainsworth, Computer Methods in Applied Mechanics and Engineering **190**(48), 6323 (2001). DOI 10.1016/S0045-7825(01)00236-5. URL http://www.sciencedirect.com/science/article/pii/S0045782501002365
58. N.P. van Dijk, International Journal for Numerical Methods in Engineering pp. n/a–n/a (2015). DOI 10.1002/nme.5198. URL http://dx.doi.org/10.1002/nme.5198
59. V.D. Nguyen, G. Becker, L. Noels, Computer Methods in Applied Mechanics and Engineering **260**(0), 63 (2013). DOI http://dx.doi.org/10.1016/j.cma.2013.03.024. URL http://www.sciencedirect.com/science/article/pii/S0045782513000832
60. M. Mosby, K. Matouš, International Journal for Numerical Methods in Engineering **102**(3-4), 748 (2015). DOI 10.1002/nme.4755. URL http://dx.doi.org/10.1002/nme.4755
61. C. Miehe, Computer Methods in Applied Mechanics and Engineering **134**(34), 223 (1996). DOI http://dx.doi.org/10.1016/0045-7825(96)01019-5. URL http://www.sciencedirect.com/science/article/pii/0045782596010195
62. J.M. Tyrus, M. Gosz, E. DeSantiago, International Journal of Solids and Structures **44**(9), 2972 (2007). DOI DOI: 10.1016/j.ijsolstr.2006.08.040. URL http://www.sciencedirect.com/science/article/B6VJS-4KW5FH7-2/2/5ff1cecbcb5cdcf33cab7c7f6f6a1935
63. J. Wismans, Computed tomography-based modeling of structured polymers. Ph.D. thesis, Technische Universiteit Eindhoven (2011)
64. Z. Yuan, J. Fish, Int. J. Numer. Meth. Engng. **73**(3), 361 (2008). URL http://dx.doi.org/10.1002/nme.2074
65. A. McConnell, S. Uma, K.E. Goodson, Microelectromechanical Systems, Journal of **10**(3), 360 (2001)
66. J. Simo, C. Miehe, Computer Methods in Applied Mechanics and Engineering **98**(1), 41 (1992). DOI http://dx.doi.org/10.1016/0045-7825(92)90170-O. URL http://www.sciencedirect.com/science/article/pii/004578259290170O

67. L. Adam, J.P. Ponthot, International Journal of Solids and Structures **42**(2122), 5615 (2005). DOI http://dx.doi.org/10.1016/j.ijsolstr.2005.03.020. URL http://www.sciencedirect.com/science/article/pii/S0020768305001319. {PACAM} {VIII} {SPECIAL} {ISSUEEighth} Pan American Congress of Applied Mechanics
68. A.L. Eterovic, K.J. Bathe, International Journal for Numerical Methods in Engineering **30**(6), 1099 (1990). DOI 10.1002/nme.1620300602. URL http://dx.doi.org/10.1002/nme.1620300602
69. A. Cuitiño, M. Ortiz, Engineering Computations **9**, 437 (1992). DOI 10.1108/eb023876. URL http://dx.doi.org/10.1108/eb023876